



Gas sensing properties and modeling of YCoO₃ based perovskite materials.

This is the peer reviewed version of the following article:

Original:

Addabbo, T., Bertocci, F., Fort, A., Gregorkiewitz, M., Mugnaini, M., Spinicci, R., et al. (2015). Gas sensing properties and modeling of YCoO₃ based perovskite materials. SENSORS AND ACTUATORS. B, CHEMICAL, 221, 1137-1155 [10.1016/j.snb.2015.07.079].

Availability:

This version is available <http://hdl.handle.net/11365/980505> since 2016-11-10T11:28:45Z

Published:

DOI:10.1016/j.snb.2015.07.079

Terms of use:

Open Access

The terms and conditions for the reuse of this version of the manuscript are specified in the publishing policy. Works made available under a Creative Commons license can be used according to the terms and conditions of said license.

For all terms of use and more information see the publisher's website.

(Article begins on next page)

Gas sensing properties and modeling of YCoO_3 based perovskite materials

Tommaso Addabbo¹, Francesco Bertocci¹, Ada Fort¹, Michele Gregorkiewitz², Marco Mugnaini¹, Roberto Spinicci³, Valerio Vignoli¹.

¹Dip. di Ingegneria dell'Informazione e Scienze Matematiche, University of Siena,
via Roma 56, I-53100 Siena, Italy
e-mail ada@dii.unisi.it

²Dip of Industrial Engineering

University of Florence, via Santa Marta 3, 50139 Florence, Italy

³Dip di Scienze Fisiche, della Terra e dell'Ambiente, University of Siena,
via Laterina 8, I-53100 Siena, Italy

Abstract

YCoO_3 perovskite powder was prepared by the classical sol-gel method, which was extended to the preparation also of non stoichiometric materials or samples containing platinum or palladium, incorporated either during synthesis or a posteriori through impregnation. The prepared powders were characterized in terms of composition and structure, using X-ray diffraction (XRD) and Rietveld refinement. The compounds show a tunnel structure with octahedral framework.

The surface properties of these powders were investigated studying their catalytic activity in CO oxidation, as well as their adsorptive features towards oxygen and their redox behavior by means of TPD and TPR respectively. Sensing films of the prepared powders were realized by a screen-printing technique. The electrical properties and response to various gases were studied and found to be correlated to composition and structure of the different materials. Moreover the influence of the microstructure was analyzed and a model was developed.

The responses to both oxidizing and reducing gases such as CO, NO_2 , NO, and CH_4 were evaluated and discussed both in an inert environment (nitrogen) and in the presence of oxygen (air). All the YCoO_3 based sensors show p-type semiconducting properties in the tested environments within the temperature range of 100–380°C. All the studied materials react to CO in the high temperature range with a limited response but a large response speed. The response to NOx is optimum in the low temperature range between 160°C and 200°C; moreover even at these temperatures both the response and the recovery time are satisfactory. The response towards CH_4 results much lower. Finally, the gas sensor properties of the proposed materials proved to be insensitive to ambient humidity.

1. Introduction

It is well known [1,2] that many metals are stable in the ABO_3 perovskite structure provided that the A (typically an alkaline earth or a rare-earth 8-12 coordinated metal ion) and B (usually a transition metal in octahedral coordination) cations have dimensions in agreement with the limits of the so-called “tolerance factor” t ($0.8 < t < 1.0$) defined by Goldschmidt [3] as $t = (r_A + r_O) / \sqrt{2}(r_B + r_O)$, where r_A , r_B , and r_O are the ionic radii for A, B, and O, respectively, and $r_A > 90$ pm, $r_B > 51$ pm.

As an addition to the variability of composition, perovskite materials can tolerate significant isomorphous substitutions and non-stoichiometry while still maintaining the perovskite structure. Perovskite-type oxide materials have therefore attracted a great interest in many applied and fundamental areas of solid state chemistry, physics, advanced materials, and catalysis.

The effects on redox, electrical and catalytic properties, which can be obtained by tuning the perovskite structure, i.e. selecting the chemical composition (choice of metals A and B), introducing some vacancies and/or partially substituting metal B, were the object of many studies, in particular as far as catalytic properties are concerned. It was seen that many of the material properties can be effectively tuned to the application exploiting the material flexibility. For instance, partial substitution of either one or both the A and B cations by other metals with similar or different oxidation states was used to increase the catalytic activity, and to promote the creation of structural defects, e.g. anionic or cationic vacancies, thus modifying the electrical properties (conductivity) of the material.

In particular, partial substitution of the A and/or B cation with a lower valence cation can force the (remaining) B-element to higher oxidation states or can stimulate the formation of oxygen vacancies. On the other hand, substitution with a cation of the same valence should not lead in principle to the above mentioned modifications, but it can induce a weakening of the M–O bond strength [4-7] with both transition and non-transition metal ions.

For instance, studying perovskites of the type $AFeO_3$, where A indicates different rare earths, the effect of substitutions at the A site was proved to be correlated with structural and redox properties by Porta et al. [2], who discussed how the variation of lattice constants, due to the ionic radii of the A cations, ($LaFeO_3 > NdFeO_3 > SmFeO_3$), may increase bond strengths.

Perovskitic materials were also deeply studied for ‘high temperature’ gas sensing applications - based on ionic conduction - due to their high melting and/or decomposition temperatures, and to their structural and morphological stability [8].

More recently many perovskitic materials have been proposed for ‘low temperature’ gas sensing applications, in which the variation of the electronic conduction induced by gas ionosorption is exploited as the basis of sensing mechanism [9-12]. In this context, $LaCoO_3$ is the most intensively studied composition [13], especially for CO sensing. This application should greatly benefit from the above mentioned mechanisms to adapt and tune the electronic structure and gas sensing properties to the target applications.

Here we present a study of novel perovskite materials based on the composition $YCoO_3$. The substitution of La (ionic radius $r^{XII} = 136$ pm, [14]) with the much smaller Y ($r^{VIII} = 102$ pm) gives rise to considerably shorter A-O bonds which cause bond energies to increase. The rationale for this choice was founded on the following observation: for ‘low temperature’ chemoresistors, the relevant chemical reactions are those which cause the trapping or releasing of carriers at the surface. Large and stable responses of conductometric metal oxide sensors rely on surface ionosorption and exploit materials showing a very low bulk oxygen mobility [15]. The proposed materials could therefore behave as more stable material in a wider range of operating temperatures with no adverse effect on the magnitude of the gas response.

In addition, we were interested to address the role of vacancies and substitutions in the chemical behavior of the products. Starting from the ideal composition YCoO_3 which was produced by a citrate sol-gel method and subsequent calcination, it was tried to provoke such modifications either varying the stoichiometry (to create A or B vacancies) or introducing, in the reaction mixture, an additional metal element to be incorporated on the octahedral (B) site. Pd and Pt dopants were selected in the attempt to enhance gas response as might be expected on the basis of results obtained for other metal oxides and recently elucidated by Hübner [16]. As an alternative, Pd and Pt were also added by impregnation of the pure ceramic which should favor the adsorption of highly reactive ionized oxygen and play a fundamental role in surface oxidation reactions [17].

Crystal structure, phase identification, chemical composition and structure of the powders were assessed using X-ray diffraction and Rietveld refinement. The surface properties were investigated through the study of the catalytic activity in CO oxidation and of the oxygen adsorption and redox behavior in temperature programmed desorption (TPD) and reduction (TPR) experiments, respectively.

Finally, in order to derive the gas sensing properties of the different developed materials and to compare their performance, conductometric sensors based on films obtained from the proposed powders were prepared, and the responses to CO, NO_2 , NO and CH_4 were measured, evaluated, discussed and interpreted with a particular attention to the different mechanisms at the basis of the sensor behavior. The obtained results were correlated with those obtained by the different characterization techniques. A particular attention was paid to the correlation of the gas sensor responses with the possible presence of pre-adsorbed oxygen suggested by the TPD results, or to the red-ox activity of the surface pointed out by the CO conversion results.

2. Experimental

YCoO_3 based powders were prepared by means of the classical sol-gel route (all reagents are Aldrich, purity > 99.9%) [1]. An aqueous solution of $\text{Y}(\text{NO}_3)_3 \cdot 6\text{H}_2\text{O}$, $\text{Co}(\text{NO}_3)_2 \cdot 6\text{H}_2\text{O}$ and citric acid in molar ratio 1:1:2 was heated keeping the temperature around 100 °C and stirring continuously for about 30 min. The solution, once heated, becomes first a sol, which then leads to the formation of a gel, gray coloured, which was dried and decomposed at 150°C, and subsequently calcined at increasing temperature (with a heating rate of 5 °C/min, and with an isothermal step of 24 hours at 350°C) up to 900°C, and maintained at this temperature for more than 48 hours. Using the same method, LaCoO_3 perovskite was also prepared in order to have a reference material whose properties are known in the literature.

With the aim to prepare defective perovskite, $\text{YCo}_{1-x}\text{O}_3$ or $\text{Y}_{1-x}\text{CoO}_3$, the molar ratio in the reaction mixture was varied with x in the range 0.01-0.1. The doped compositions $\text{YCo}_{1-x}\text{Pd}_x\text{O}_3$ and $\text{YCo}_{1-x}\text{Pt}_x\text{O}_3$ were prepared by adding small quantities ($x = 0.03$ to 0.1) of Pd(II) nitrate or acetate and Pt(II) acetylacetonate to the mixture of Y and Co nitrates followed by the heating and calcination steps as above.

Impregnated products were prepared by soaking YCoO_3 or defective perovskites in an aqueous solution of $\text{Pd}(\text{NO}_3)_2$, $\text{Pd}(\text{CH}_3\text{COO})_2$ or $\text{Pt}(\text{acac})_2$. The salts of the metals, kept dried under vacuum, were dissolved in distilled water or acetone, the solution added to the perovskite powder in a mass ratio varying between 0.005 and 0.01, and the mixture was then dried in a muffle in a temperature range between 500°C and 650°C for a time ranging from 6 to 18 hours. These products are hereafter indicated with the name of the starting material followed by '+Y x wt%', where Y can be Pd or Pt, and x is the mass ratio between the Y salt in the solution and the perovskite.

For X-ray diffraction experiments, the powders were gently ground in an agate mortar to break agglomerates. Further grinding was not necessary considering the small grain size ($<1 \mu\text{m}$ see section 3.1) resulting from the synthesis procedure. A Philips PW1050/PW1710 powder diffraction goniometer with Bragg-Brentano geometry was used, operating with $\text{CuK}\alpha$ radiation (long fine focus, $\lambda_1=154.0598$, $\lambda_2=154.4418$ pm), a secondary beam graphite monochromator and a proportional counter. Patterns were obtained for diffraction angles 2θ ranging from 4° to 70° for routine work and from 4° to 132° for samples intended for more quantitative structural characterization using Rietveld refinement.

Full pattern Rietveld refinements were performed using the GSAS software package [18] combined with the EXPGUI graphical user interface [19]. Refined overall parameters comprised 15 to 21 background coefficients, a linear correction term to account for displacement of the origin of the diffraction pattern, a global, angle independent Gaussian broadening term [20], and two Lorentzian broadening terms which are specific for each phase in the product mixture and give an estimate of their grain size (X , Scherrer broadening) and lattice distortions (Y , microstrain broadening).

Bragg intensities of the calculated pattern contain a set of scale factors which were refined for each phase composing the mixture and then converted to abundances in terms of mass fractions. Unit cell and atom positions were taken from literature for the perovskite phase YCoO_3 and the identified impurities yttria Y_2O_3 , Co-spinel Co_3O_4 , Pd and PdO [21-29]. During least-squares refinement, the unit cell parameters were allowed to refine for all phases in the mixtures, while the atom parameters of the minority components (Y_2O_3 , Co_3O_4 , Pd, PdO) were kept at their original values throughout.

The catalytic activity, surface reduction and oxygen desorption of the prepared materials have been studied by means of a continuous flow tubular reactor where 0.05 – 0.1 g of perovskite powder was placed and the temperature could be controlled in the range 100°C – 800°C . Test gases were passed over the catalyst at a controlled and constant flow rate of 24 mL/min, and the outlet gas was analyzed by means of a Perkin Elmer Autosystem gas chromatograph equipped with hot wire detector and capillary columns.

The catalytic activity was investigated in the range 80°C – 250°C according to the type of catalyst, increasing the temperature stepwise. For CO conversion measurements, the samples were pretreated by heating at 450°C in He + O_2 (20% O_2) and subsequently cooled to the reaction temperature; the reaction was performed by injecting a mixture of He + CO (2 % CO) and O_2 (20%).

TPD measurements were performed by pretreating the samples in a flow of He + O_2 (20% O_2) for 1 h at 450°C and subsequently cooling them to room temperature. The sample was kept at room temperature under the same gas flow for 1 h, after this time a flow of pure helium was fed in the reactor and the measurement started while the temperature of the catalyst was progressively increased at $8^\circ\text{C}/\text{min}$.

For TPR measurements the samples were pretreated in the same way as in TPD experiments. Once at room temperature, the samples were kept in the same gas flow for 1 h, after this time a flow of He + H_2 (10% H_2) was fed into the reactor and the measurement started while the temperature of the catalyst was progressively increased at $8^\circ\text{C}/\text{min}$.

Figure 1 about here

In order to assess the gas sensing properties of the prepared materials, prototype gas sensors were realized by the screen printing technique depositing a thick film obtained from the different perovskite powders. A printable ink was obtained by mixing the metal oxide powders with an organic vehicle (dimethylphtalate), and by adding some percents of glass frit. The ink was deposited between Ag electrodes on an alumina substrate hosting also a Pt temperature sensor and a heater (Figure 1). After film deposition the devices were fired up to 600°C for some hours. The morphology of the oxide powders and the thick films was analyzed by scanning electron microscopy (SEM).

Resistance measurements were performed in a steel chamber under a constant gas flow of 200 mL/min. The characterization of the gas sensor response is obtained in terms of both temperature and concentration dependence through a fully automated measurement system [30]. Sensors were tested under a constant gas flow with CO mixtures in dry and humid air and nitrogen as carrier gases. Some tests with interfering gases were also performed. In particular CH₄, NO and NO₂ mixtures were used. In this work the sensor response is defined as follows:

$$Resp=(R-R_0)/R_0 \quad (1)$$

where R_0 is the baseline resistance value obtained at the considered temperature in a carrier gas, whereas R is the value of the sensor resistance after an exposure of fixed duration to the test gas mixture.

3. Results and discussion

3.1. Product identification and structural characterization

A total of 45 products covering 14 compositions have been synthesized. In all cases, a mixture was obtained and the predominant phase was a perovskite where composition was modified systematically to be either stoichiometric (YCoO₃), defective ((Y,□)CoO₃ or Y(Co,□)O₃), substituted (Y(Co,Pd)O₃ or Y(Co,Pt)O₃) or impregnated (perovskite + Pd or perovskite + Pt).

For our purpose it was important to fully characterize the synthesized ceramics with respect to phase composition, crystallite size and crystal structure. All of them were therefore submitted to X-ray powder diffraction to identify the crystalline phases in the mixture, and Rietveld refinement was undertaken for representative products with a high (>80%) content of the perovskite phase (Table I).

3.1.1. Crystal structure refinement of YCoO₃ perovskite

The reference perovskite phase YCoO₃, corresponding to stoichiometric Y:Co=1:1 batch compositions, was reproducibly obtained if calcination was sufficient (900°C/2d, 8 out of 16 trials). The perovskite content of these products varies from 93 to 98% and is accompanied by small amounts of yttria Y₂O₃ (0-6%) and spinel Co₃O₄ (0-5%).

In order to get precise information about the structural and microstructural details of this series of products, Rietveld refinement was conducted using four samples (batch #1-4, Tables I and II). The first two (#1 and #2) were taken from an early stage of the synthesis procedure (850°C/5h for

#2) and show high contents of the binary oxides Y_2O_3 and Co_3O_4 (~10 wt% each as compared with less than ~4 wt% of total impurities for the mature counterparts #3 and #4, Table I).

Regarding the perovskite phase itself, there were no systematic differences between the four samples as is nicely demonstrated by the unit cell volume ($205.5 \pm 0.1 \text{ \AA}^3$, Table II) which would be very sensitive to structural changes. With regard to the microstructural parameters X (Scherrer broadening) and Y (microstrain broadening), X lies within 2σ and Y within 5σ of the corresponding values for samples #3 and #4 and differences are possibly due to the shorter 2θ interval ($4-70^\circ$) used for samples #1 and #2 which is insufficient for a proper determination of Y .

Figure 2 about here

For products #3 and #4, high quality diffraction patterns (see Experimental, section 2) were recorded to be used in the refinement of the reference $YCoO_3$ crystal structure. Refinement converged with a very low residual error of Bragg intensities ($RF2(YCoO_3)=0.027$) which reflects the excellent agreement between the calculated and observed patterns reported in Figure 2 and warrants a high accuracy of the structural results.

Table I about here

Table II about here

The most important parameters for the present work are resumed in Tables I and II and will be discussed together with the remaining samples. The structure is very similar to the one found from neutron powder diffraction at 300 K (Knížek et al., [25]). In particular, the average Co-O bond length is, in both studies, 193.3(2) pm as expected from ionic radii (54.5 pm for six-coordinate low-spin Co^{3+} and 138 pm for 4-coordinate O^{2-} , [14]). Table II reports the dispersion (1.2 pm) of the individual Co-O distances contributing to the average. This dispersion (1.6 pm in [25]) is considerably larger than the uncertainties (0.2 pm) of the individual contributing distances and means a slight shortening of the octahedra along the c axis. The distortion does not change up to 900 K so that no Jahn-Teller effect was inferred although above 600 K a transition to intermediate and high spin states of the $Co^{3+} 3d^6$ ion has been observed in thermal expansion and magnetic susceptibility data [25]. These facts should be considered for operation of our sensors at high temperatures.

An interesting result, qualitatively new, which could not be obtained in earlier work based on neutron diffraction [23,25], refers to microstructure. The Scherrer broadening of $X=2.3$ cdeg (sample #3, Table I) is at the lower end of what can be obtained on laboratory diffraction equipments, even using highly crystalline standard materials. This corresponds to an estimated average domain size of ~400 nm. Note that a grain is usually made up of several coherently diffracting domains, therefore this data should be considered as an estimate of a lower limit which is compatible with the grain size observed in SEM images (see Fig. 3 where grains smaller than ~1 μm can be seen), and will be useful as a reference value. The consequence on gas sensing of the presence of such small grains will be discussed in the following, where the impact on the sensor behavior of the presence of nanoparticles will be demonstrated.

More important, in absolute terms, appears the microstrain parameter ($Y=9.4$ cdeg, Table I) which is about twice the value for a silicon standard and cannot be attributed to instrumental broadening. One reason for microstrain may be the presence of vacancies or extended defects.

It should also be mentioned that in no case, neither in the stoichiometric perovskites (#1 to #4, this section) nor in the samples of the following section, was there an appreciable content of amorphous components.

Figure 3 about here

3.1.2. Defective and substituted YCoO_3 perovskites

Starting from the above results about the stoichiometric products, we analyse the evolution of crystal and microstructure of the materials where vacancies and cation substitutions are inferred from the synthesis procedure.

Both vacancies and substitutions at the Co or Y site can, in principle, be recognized from the site occupation factor *SOF*. Inspection of the corresponding values in Table II shows that most of them lie near the expected value for the ideal stoichiometry $\text{SOF}(\text{Co}) = \text{SOF}(\text{Y}) = 1$, and there is no systematic deviation which would indicate the presence of Co vacancies inferred from the batch compositions. The only, very clear, exception is the Pt-containing perovskite where $\text{SOF} = 1.15$ is 8σ away from unity and indicates the presence of a heavier scatterer at the Co site. A simple conversion using the number of electrons gives an estimate of the degree of substitution $x = (1.15 - 1)27 / (78 - 27) = 0.08(1)$ which comes close to $x = 0.05$ as expected from synthesis.

Similarly, the unit cell volume of the Pt-substituted perovskite ($V = 207.74 \text{ \AA}^3$) is much larger (by $>100\sigma$) than the others which cluster around a mean of $\langle V \rangle = 205.48(8) \text{ \AA}^3$, as a consequence of the size of the Pt ion (62.5 pm for $^{\text{VI}}\text{Pt}^{4+}$) which is 8.0 pm larger than $^{\text{VI}}\text{Co}^{3+}$. Taking $x = 0.1$, we would expect an increase of 0.8 pm in the octahedral Co-O distance, and indeed, we find $194.4(2) \text{ pm}$, which is 0.9 pm larger than the mean of the remaining Co-O distances ($193.5(2) \text{ pm}$, Table II). This model, with Pt at the B-site, is in accordance with the Goldschmidt criterion (see above) and previous results for Pt-containing perovskites [31-34] where Pt^{4+} -O octahedral distances of $200\text{-}203 \text{ pm}$ have been found. Furthermore, substitution with Pt^{4+} corresponds to p-type doping, again in accordance with experiment (see section 3.4 of this study).

In view of these results, there is no doubt that the Pt doped perovskites contain all Pt at the octahedral position where it substitutes about $x = 0.1$ Co ions as inferred from the above. Assuming random Co-Pt distribution, the size difference should cause considerable lattice strain. A high microstrain broadening ($Y = 26$ cdeg as compared to ~ 10 cdeg for the remaining perovskites, Tab. II) confirms this hypothesis, i.e. Pt substitution might trigger another factor, beside electron configuration, which should be considered when discussing materials properties in catalysis and chemical sensing.

Palladium is similar in size to Pt, having an ionic radius of 61.5 pm for $^{VI}Pd^{4+}$, and contributes with 46 electrons to scattering. However, none of the relevant parameters (unit cell volume, Co-O distance, *SOF*, see Table II) indicates a significant deviation from the values for the non-substituted perovskites. On the contrary, the result of quantitative phase analysis (Table I) shows that Pd appears in the separate phases Pd and PdO. Mass percentages of these phases increase with Pd doping during synthesis, and correspond to about 0.050 and 0.026 Pd for samples #12 and #28, respectively, i.e. half of the molar amount expected ($x=0.1$ and 0.05) from batch composition. The errors at these low levels of concentration are relatively high (see Table 1), and we prefer to conclude that most, if not all, Pd is probably outside the perovskite where it adopts a more reduced state (+2 in PdO and 0 in Pd). Nonetheless it will be shown in the following that Pd doped materials have a specific redox and electric behaviour, which could be compatible with a certain degree of incorporation of $^{VI}Pd^{2+}$ or $^{VI}Pd^{3+}$ in the perovskite.

There is much ongoing discussion about the incorporation of Pd in the perovskite structure, especially after the discovery [35] that Pd uptake and decomposition in the $LaCoO_3: Pd$ system is reversible at $\sim 800^\circ C$ depending on the redox conditions, with important implications for exhaust gas catalysis. Kim et al. [36] resolved the crystal structure of a stoichiometric $LaPdO_3$ where palladium occurs in the trivalent state with an interatomic Pd-O distance of 208(2) pm, 15 pm larger than Co-O. In most other cases (e.g. [35-38]), Pd was found along with Fe, Co etc as a solid solution at the B site so that, even if EXAFS/XANES data suggested a somewhat higher oxidation complying with a shorter Pd-O distance, substitution should cause considerable strain. Together with the strong tendency of Pd for other coordinations, this suggests again that Pd-doped perovskite is unstable (a hypothetical $YPdO_3$ would have the Goldschmidt factor $t=0.81$ at its lower limit), and it is possible that our material has initially formed as a solid solution and then decomposed during calcination at higher temperatures, similar to the observations [37] for Pd-doped $LaCoO_3$. During decomposition, the grain size would have been reduced, and this is indeed supported by the significantly higher Scherrer broadening ($X=3.8$ instead of 2.3 cdeg for the other samples, Table I).

Regarding the defective compositions $(Y, \square)CoO_3$ and $Y(Co, \square)O_3$, no particular trend can be recognized except that the binary oxides in excess seem to prefer forming separate phases instead of a defective perovskite (Table I), with the only exception of sample #F63. The composition $Y_{1+x}Co_{1-x}O_3$ of the resulting perovskites, if the loss of Y and Co to the binary oxides is considered, can be calculated to tend towards a small deficiency in Co ($x \approx 0.03$, considerably less than $x=0.1$ inferred from batch), except for $(Y, \square)CoO_3$ where $x \approx 0$. In Table I we therefore refer to these materials using the general expressions (Y, \square) and (Co, \square) , while in the remainder of this study, we use the nominal composition from batch merely for the purpose to identify the sample.

3.2. CO conversion

The catalytic activity in terms of CO oxidation of the prepared materials is shown in Figure 4. It can be seen that CO conversion increases slowly and reaches large values in the temperature range $100^\circ C - 200^\circ C$ for all the tested materials.

In the following we choose the parameter $T_{50\%}$ (temperature at which the catalytic activity reaches the 50% conversion) as a parameter capable of summarizing the catalytic activity of a sample, and get the following results.

$YCoO_3$ has a $T_{50\%}$ of about $180^\circ C$. The Co-defective materials, such as $YCo_{1-x}O_3$, show a similar behavior but a $T_{50\%}$ slightly higher and a larger conversion at $200^\circ C$. Also the samples doped with Pd, $YCo_{1-x}Pd_xO_3$, show a behavior similar to cobalt defective materials and a similar $T_{50\%}$ as long as the content of Pd is below 5%. With larger contents of Pd larger amounts are on the surface as

metallic Pd or PdO (see Table I) and the behavior becomes very similar to the samples impregnated on the surface with 1 wt% of Pd or Pt. These samples show a different behavior, in particular the samples containing Pd pass from a conversion of about 20% to a conversion of almost 100% over a 15°C temperature range between 150°C and 165°C (a similar behavior was observed for $\text{LaCo}_{1-x}\text{Pd}_x\text{O}_3$ in [39] and the references therein), while the samples containing Pt show the same behavior in the range between 125°C and 140°C.

Figure 4 about here

3.3. Temperature programmed desorption (TPD) and temperature programmed reduction (TPR) experiments.

TPD and H_2 -TPR can provide some information, such as the oxidability of the metallic ions, the activity of the surface and lattice oxygen ions, and the stability of the material. The TPD- O_2 profiles of perovskite-type oxides usually exhibit two oxygen desorption peaks (LaCoO_3 , [40]): a first one located at low temperatures due to adsorbed oxygen (α -type), and a second one placed at high temperatures associated to lattice oxygen (β type). In particular, for similar materials, a desorption peak at $T < 350^\circ\text{C}$ was attributed to O_2^- and a desorption peak at $350^\circ\text{C} \leq T \leq 750^\circ\text{C}$ to peroxide ion $\text{O}_2^{2-}/\text{O}^-$ whereas, as already said, the desorption peak at $T \geq 750^\circ\text{C}$ is attributed to lattice oxygen ion O^{2-} . The presence of peaks related to oxygen chemisorption can be very important since, in the literature, classically the low temperature chemoresistive behavior is completely explained by the presence of highly reactive surface peroxide ions. Recently it was pointed out that in many cases the sensor response is partially or completely due to direct chemisorption of the target gas on the surface [41-46]. So the presence/absence of low temperature peaks does not completely describe the gas sensing properties of the material under study. In any case it is very important to use the TPD analysis to evaluate, for instance, the material stability.

As shown in Figure 5, YCoO_3 (and, as expected from structural characterization, the nominally Y-defective material) only display the high temperature desorption peak (β type oxygen). It should be noted, in any case, that weakly adsorbed species could have been desorbed at low temperature during the pretreatment.

Samples with free Pt/Pd (including the Pd-doped perovskites, as it can be seen in Figure 5), show large desorption peaks at relatively low temperatures, except for the lowest concentrations of Pd which seems less effective anyway. This indicates the presence of surface adsorbed oxygen species (possibly chemisorbed and reactive). Some smaller peaks at low temperatures appear also when analyzing the defective powders. The lowest Pd-doped perovskite, $\text{YCo}_{0.97}\text{Pd}_{0.03}\text{O}_3$, behaves similarly to the Co-defective material, exhibiting the high-temperature peak at somewhat lower temperature ($\sim 700^\circ\text{C}$), in agreement with the conclusions drawn from Rietveld refinement (section 3.1.2).

From these results all the prepared materials seem good candidates for the realization of gas sensors because they don't lose lattice oxygen in the working temperature range, moreover the addition of Pd and Pt could improve the operation at lower temperature because, as expected, the metals promote the formation of adsorbed oxygen species.

Figure 5 about here

During H₂-TPR analysis, the metal ions with high valence are reduced to the ions with low valence or metal atoms by H₂; both the surface oxygen ions and the lattice oxygen ions participate in the reduction reaction. Therefore, the reduction peaks reflect not only the oxidizability of the metal ions but also the activity of oxygen species.

In Figure 6 the results of TPR for some prepared powders are shown. As it can be seen in the lowest plots, YCoO₃ perovskite shows two overlapping reduction peaks with maxima at about 400°C and 550°C, respectively. Similarly to what happens for LaCoO₃ [47], these can be attributed respectively to the reduction of Co³⁺ to Co²⁺ and Co²⁺ to Co⁰ (remember that at these temperatures Co³⁺ undergoes transition from the low to a higher spin state). A somewhat lower position of the high temperature peak is observed in Co-defective powders and powder with Pt/Pd metal on the surface (see Figure 6 lower and middle plots). The position of the high temperature peaks indicates that the reduction of the surface by reaction with β species occurs below 600°C but above 350°C, this sets the operating range for conductometric gas sensors.

Pd/Pt doped perovskites show a shift of the high temperature peak toward low temperatures with respect to pure YCoO₃ (see upper plots in Figure 6); this improved reducibility can be due to the presence of palladium or platinum atoms or ions, or to the fact that palladium or platinum as such, as discussed in section 3.1.2, provoke a smaller grain size or introduce distortions of the lattice causing a decrease of the lattice energy and therefore facilitating the surface reduction (as already discussed for LaCoPdO₃: [39] and the references therein).

All the powders modified by Pd (and somewhat less those with Pt) show some peaks at low temperatures (200°C-300°C), and this probably corresponds to the reaction with α-oxygen species [47] (revealed also in TPD experiments by low temperature desorption peaks, see Fig.5). This behavior is shown by the materials that act as CO oxidation catalysts at the lowest temperatures (see section 3.2). These peaks for impregnated powders are very broad, indicating that the oxygen released at low temperatures is adsorbed on several different sites of the catalyst surface [39].

As already stated, the mechanism of reduction, which doesn't involve the lattice oxygen, is the most useful for 'low temperature' chemoresistive sensor development. From this point of view TPR results enforce the idea that doped and Co defective YCoO₃ could behave better for the sensing of reducing gases.

Figure 6 about here

3.4. Gas sensing properties assessment

Sensors based on the perovskite powders were tested; the microstructure of the sensing films is shown in Figure 3. In what follows the experimental results concerning samples of defective, Pd/Pt doped, and Pd/Pt impregnated materials and the reference YCoO₃ are reported. For each material at least three sensors were tested; the results obtained for each set of sensors from the same material are repeatable within the tolerance related to the production process (20%). Hereafter, for each material the data of only one sensor are reported.

All the materials behave as p-type semiconductors, this points out the prevalence of intrinsic bulk acceptor defects such as metal vacancies (probably Co) as discussed in section 3.1.2 and found for similar perovskitic materials [47].

To test and understand the performance of the developed sensors, the baseline value of resistance in the carrier gases at different temperatures is studied.

The baseline values of the resistance in air are shown in Figure 7 for the different materials. It can be seen that the presence of defects causes a reduction of the resistance baseline value with respect to the one of the stoichiometric material: this indicates that it actually introduces extrinsic acceptor

energy level and enhances the free carrier density. The same behavior was found for Pt doped materials, and this reinforces what already suggested by the analysis in section 3.2.1: Pt enters the lattice probably as Pt^{4+} , in connection with oxygen excess or Co^{2+} excess. This corresponds to p-type doping, because Pt^{4+} can pass to Pt^{2+} taking two electrons. Note that if Pt is in the crystal as Pt^{2+} this corresponds to introduce n type defects, in connection for instance with oxygen vacancies.

In figure 7 it can be seen that the baseline resistance of Pd doped material is much larger than the one of the stoichiometric material. This fact can be justified by the introduction of donor impurities, so even if no evidence of Pd entering the lattice comes from the analysis in section 3.2.1, there is an indication of n-type doping, hence a part of Pd could enter the lattice as Pd^{2+} or Pd^{3+} while a larger amount segregates on the surface as metal or PdO [35]. Note that in the lattice we can have in principle Pd^{2+} , Pd^{3+} or Pd^{4+} , and these oxidation numbers can be accompanied, respectively, by oxygen vacancies, stretching of M-O bonds, and Co^{2+} or oxygen excess. The first and the second ions behave as n-type defects.

Usually the relationship between temperature and resistance for metal oxides can be written as follows:

$$R = R_f e^{\frac{qV_s}{kT}} \Rightarrow \ln\left(\frac{R}{1\Omega}\right) = \ln\left(\frac{R_f}{1\Omega}\right) + \frac{qV_s}{kT} \quad (2)$$

Where q is the electron charge, k is the Boltzmann constant, T is the absolute temperature whereas R_f is a pre-exponential factor weakly depending on temperature and related to the sensor structure/geometry. The activation energy qV_s is interpreted as a potential barrier established at the grain surface due to localized charged species, which can be either intrinsic surface defects or ionized adsorbates [41]. This relationship is usually adopted to describe a situation where all the bulk impurities are ionized. On the other hand it must be considered that the exponential relationship with temperature can also describe the incomplete ionization of the extrinsic impurities (acceptors), being in this case qV_s interpreted as the energy gap between the valence band top level and the acceptor level. Some experiments performed by the authors, similar to those presented in [48], seem to point out that the bulk acceptors are completely ionized above 150°C and that the most probable interpretation of qV_s is an intrinsic potential barrier originated by a population of surface defects acting as acceptors.

Figure 7 shows the resistance log as a function of $1/T$ in synthetic air, highlighting an almost linear behavior in the temperature range used for measurements (200°C-320°C). This corresponds to an almost constant value for qV_s (eV) in the considered conditions showing that the surface barrier and the charge trapped at the surface do not significantly vary in the different tested environmental conditions.

This is an unexpected fact, since usually for gas sensing materials, and especially for other perovskite materials, the potential barrier height in air significantly varies in the range 200°C and 300°C due to the variation of chemisorbed oxygen density [49]. In particular, above 200°C the presence of oxygen should decrease the barrier height due to formation of adsorbed O^- .

The estimated values of the activation energy for the different materials are very close with the exception of the value found for Pd doped materials, which are significantly larger.

The value of the activation energy for both the base material and the defective ones, $E_a = qV_s$, is close to 0.55 eV. This value is much lower than the energy gap of YCoO_3 that was estimated to be 1.84 eV [50]. It is instead more similar to the value $E_a = 0.3$ eV found by Liu in [51], which in that paper was attributed to an extrinsic acceptor level (dopant Ca).

In detail, as a comment to Figure 7, the qV_s value for defective and stoichiometric materials is similar. On the other hand, as already stated, the Pd doped materials show an activation energy

higher than the stoichiometric material, especially at high temperature. This fact could be related to the introduction of a donor level that up shifts the bulk Fermi level (and this strengthens the hypothesis of some Pd incorporated in the structure), but more probably to an increased density of intrinsic acceptor surface defects. The materials impregnated with Pd and Pt have activation energies similar to the defective material, in this case a different behavior as a sensor will be due only to the promotion of chemisorption on the surface.

Figure 7 about here

It can also be noted that the value of baseline resistance in air and in nitrogen are quite close. A similar result was found also for LaCoO₃ in [46].

The closeness of the resistance value in air and in nitrogen, as shown in Figure 8, points out that only a very small amount of ionized species is formed on the surface due to the presence of air. The low or negligible presence of ionized adsorbed oxygen species in the considered temperature range is in accordance with data both from TPD and TPR as far as stoichiometric material is concerned, where no desorption of oxygen was seen up to high temperatures (over 500°C) and no reduction peaks at low temperature are observed. On the other hand, for most Pd and Pt containing materials, in TPR experiments reduction of the surface was observed also at lower temperatures, i.e. in the temperature range used for gas sensing characterization. This oxygen was interpreted as adsorbed oxygen, possibly chemisorbed, that in principle could strongly contribute to the sensing mechanism. Instead also for Pd and Pt containing materials the base line resistance values in air and nitrogen are close, showing little effect of oxygen on sensor conductivity. This could indicate that the largest part of the adsorbed oxygen is neutral and doesn't contribute to sensing, so that the sensing properties of these doped material are only marginally modified with respect to those of the base material.

Figure 8 about here

3.4.1 Influence of film microstructure on gas sensing

For metal oxide sensors the qV_s value in eq.(2) is considered [41] proportional to the square of adsorbate surface density, thus explaining the sensing mechanism. This relationships comes from the assumption of large grains. For the developed materials, as it can be observed in Figure 3, the grain diameter can be lower than 1 μm . This size can't be considered large with respect to the Debye length.

It is worth recalling that the Debye length is a parameter describing the scale of the depleted region in the material. Generally speaking, this quantity is defined as the length in which mobile charge carriers screen out an external electric field; some Debye lengths away from the surface the bulk density of carriers can be found again. So if the radius of the grain is much larger than the Debye length, we can assume to have a core maintaining the bulk characteristics, and a depleted region surrounding it. If the core is very large a Poisson equation in one dimension can well describe the electric field caused by the surface charge, otherwise, as already discussed, the microstructure geometry has to be taken into account. The Debye length (λ_D) is not a characteristic of the considered intrinsic semiconductor, but of the 'doped' material; λ_D is given by the following expression:

$$\lambda_D = \sqrt{\frac{\epsilon kT}{q^2 |p_b - n_b|}} \quad (3)$$

In eq. (3) ϵ is the dielectric constant whereas $|p_b - n_b|$ is the net bulk density of carriers, being p_b the density of holes and n_b the density of free electrons. These densities, especially for large band gap materials, are mainly determined by the density of ionized bulk defects.

According to this relationship, λ_D grows with increasing temperature, but it decreases increasing of the bulk defect density. That means that the ratio between the depletion region width and the crystallite geometric dimension depends on the bulk defect density. Differently from what happens in microelectronics semiconductor manufacturing, where dopants are intentionally introduced in a very regular lattice with a known and designed concentration, when preparing metal oxides for sensors development the defect density is not a priori known nor it is a design parameter. For instance, the values of the density of donors given in the literature for SnO_2 range from 10^{13} up to 10^{20} cm^{-3} , so the Debye length values can be very different depending on the preparation route, and vary from about $1 \mu\text{m}$ down to less than 1 nm at $250 \text{ }^\circ\text{C}$ (more typical values are in the range from tens to hundreds of nanometers).

If we use the value of defect density found in the literature for YCoO_3 prepared by sol gel with a route analog to the one used in this work [51,52], that is a density of $6.1 \times 10^{14} \text{ cm}^{-3}$ (at $25 \text{ }^\circ\text{C}$), we get that the Debye length λ_D is $0.50 \mu\text{m}$ at 300°C and $0.46 \mu\text{m}$ at 200°C . Also considering a higher value of carrier density, more reasonable for the used temperature range, such as 10^{16} cm^{-3} λ_D is $0.13 \mu\text{m}$ at 300°C and $0.11 \mu\text{m}$ at 200°C . For this reason we have to consider the hypothesis of small grains, and we expect a behavior different from other perovskitic material [53].

As discussed above when the grain dimension goes below a certain critical dimension [54] the influence of the grain geometry becomes important and strongly influences the sensor response. In a previous work the case of nanowire was treated by the authors [44]. In what follows the case of spherical grains will be briefly discussed in order to point out that the reduction of the sensing film grain size dramatically changes the behavior, not always giving a better performance in terms of response with respect to large grained films.

Let's consider a spherical particle of homogeneous material, let's call R_g the sphere radius: if we consider to have a certain amount of charge localized at the surface due to the presence either of intrinsic ionizable defects and of chemisorbed molecules with a total surface density N_s , than we expect, when the equilibrium is reached, that an electric field establishes in the grain to counterbalance the diffusion of free carriers which are attracted or rejected from the bulk toward the surface or vice versa. Let's consider a p-type semiconductor where the bulk hole density is p_b and the free electron density is negligible. Let's consider to have a depleted surface, that means to have a positive charge trapped at the surface, so that qN_s , the charge density, is positive and uniform on the surface. In these hypotheses the trapped charge causes the formation of a depleted negative charged layer below the surface extending to the inner of the grain and of an electric field that hinders the movement of holes from the inner to the surface. The negative charge density, ρ , in the grain at the thermal equilibrium can be found by balancing the diffusion current related to the charge density gradient and the hole drift current driven by the electric field. Considering an homogeneous grain and a uniform charge density at the surface all quantities expressed in spherical coordinates depend only by the distance from the sphere center r , so the charge density can be found from the following equations:

$$J_{tot}(r) = \sigma_p E(r) - qD_p \frac{\partial p(r)}{\partial r} = 0; \quad (4)$$

Where J is the current density, E the electric field, $\sigma_p = qp(r)\mu_p$ is the hole conductivity and μ_p is the hole mobility, D_p is the diffusion coefficient of holes and $D_p = \mu_p kT/q$, and $p(r)$ is the hole density.

Moreover the following relations can be written:

$$p(r) = p_b + \frac{\rho(r)}{q} = p_b - \frac{|\rho(r)|}{q}; \quad (5)$$

$$\sigma_p = p(r)\mu_p q = \mu_p q (p_b - \frac{|\rho(r)|}{q}); \quad (6)$$

$$E(r)\epsilon r^2 = \int_0^r \rho(u)u^2 du; \quad (7)$$

Where ϵ is the electric permittivity.

Substituting the expression in eqs. (5-7) in eq. (4) we obtain the following integral-differential equation:

$$\mu_p (qp_b - |\rho(r)|) \int_0^r |\rho(u)|u^2 du = \epsilon D_p r^2 \frac{\partial |\rho(r)|}{\partial r} \quad (8)$$

Where $0 \leq |\rho(r)| \leq qp_b$ and $\rho(0)$ assumes a value that grants the following electro-neutrality condition:

$$4\pi \int_0^{R_g} \rho(u)u^2 du = 4\pi R_g^2 q N_s. \quad (9)$$

These two equations can be solved numerically and some results are shown in Figure 9. For numerical evaluation the bulk density of holes is considered 10^{16} cm^{-3} , and the electrical parameters of YCoO_3 are taken from [51].

Eq. (8) can be rewritten as follows:

$$|\rho(r)| + \frac{\epsilon D_p r^2}{\mu_p \int_0^r |\rho(u)|u^2 du} \frac{\partial |\rho(r)|}{\partial r} = qp_b \quad (10)$$

It could be noted that since $|\rho(r)|$ is always a growing function with r , its local slope is determined by the length:

$$\lambda(r) = \frac{\epsilon D_p r^2}{\mu_p \int_0^r |\rho(u)|u^2 du} \quad (11)$$

Which takes the minimum value given by the following inequality:

$$\lambda(r) \geq \frac{3\epsilon D_p r^2}{\mu_p r^3 q p_b} = \frac{3k\epsilon T}{q^2 p_b r} \geq \frac{3k\epsilon T}{q^2 p_b R_g} \quad (12)$$

So if the radius R_g of the sphere is not much larger than the minimum value of λ which is:

$$\lambda_c = \frac{3k\epsilon T}{q^2 p_b R_g} \quad (13)$$

$|\rho(r)|$ slowly grows inside the grain and its behavior is very far from the ‘fully depleted layer approximation’ i.e. , $|\rho(r)|=0$ in the bulk and $|\rho(r)|=qp_b$ in the superficial depleted layer. On the other hand if R_g is more than 100 times the critical value in eq.(13) we find, from numerical simulation results, that the usual approximation of full depletion of the layer under the surface holds. It can be seen in Figure 9 that if the condition is met we have approximately a depleted layer with charge density $-qp_b$, and with a depth w given by the following:

$$w = R_g - R_w = R_g - \left(R_g^3 - \frac{3N_s}{p_b} R_g^2 \right)^{1/3} \quad (14)$$

In this case the potential barrier is given by this expression:

$$V_s = |V(R_g) - V(R_w)| = \int_{R_w}^{R_g} E(r) dr = \frac{qp_b}{6\epsilon} \left(R_g^2 - 3R_w^2 + 2\frac{R_w^3}{R_g} \right) \quad (15)$$

moreover if $3N_s/R_g p_b \ll 1$, i.e. far from full depletion of the grain, the potential barrier height can be approximated by the usual value found for large grains $qN_s^2/(2\epsilon p_b)$.

If the value of $N_s \approx R_g p_b/3$ the grain is completely depleted, the charge density is almost constant $\rho(r) \approx 3 qN_s/R_g \approx qp_b$ the grain conductance becomes negligible and the solution of eq.(8) gives again results that are very close to the fully depleted layer approximation, so for high values of N_s the two treatment give similar results.

Note that the inequality:

$$R_g > 100\lambda_c = 100 \frac{3k\epsilon T}{q^2 p_b R_g} \quad (16)$$

is equivalent to the following:

$$R_g > 10 \sqrt{\frac{3k\epsilon T}{q^2 p_b}} = 10\sqrt{3}\lambda_D \quad (17)$$

As expected, the condition we found is related to the Debye length λ_D .

If the charge on the surface is negative instead of positive the field is reversed with respect to the previous case, the surface density of free carriers is enhanced [41], the charge density is positive, $qp_b \leq \rho(0) \leq 3 qN_s/R_g$ and eq.(8) becomes:

$$\mu_p (qp_b + |\rho(r)|) \int_0^r |\rho(u)| u^2 du = \epsilon D_p r^2 \frac{\partial |\rho(r)|}{\partial r} \quad (18)$$

Once found the charge density in the grain, to derive the conductance of the grain it is not easy unless the large grain approximation holds.

In Figure 10 (lower plots) an approximate value for the grain conductance is plotted and compared with the one obtained under fully depleted layer approximation.

To obtain this plots the approximate conductance value is obtained as follows:

$$G_{grain} = \gamma \bar{p}(r) e^{-\frac{qV_s}{kT}} \quad (19)$$

Where $\bar{p}(r)$ is the hole density averaged in the grain, whereas γ is a geometrical parameter proportional to the depleted region width.

Note that if the grain is close to full depletion a decrease of gas response is expected, because the sensing mechanism is close to the saturation. For a p-type oxide this can reduce the response to reducing gases and a better performance with oxidizing gases is expected. When reducing gases are the target, since the Debye length depends both on temperature and on bulk defect density it is of the utmost importance to tune the material in order to have a low operating temperature and high bulk hole density (defective and p-type doped materials).

Figure 9 about here

Figure 10 about here

3.4.2 Gas sensing properties assessment.

In this section the gas sensing properties will be assessed by means of both oxidizing and reducing gases, and will be correlated with the results of the previous analyses in order to gain an insight to the sensing mechanisms that can be considered also for different metal oxides.

The concentration range for each test gas is selected in accordance to the limits set by EU regulations for environmental monitoring.

The tests were performed using at least 3 sensors for each material. Each measurement cycle was repeated at least three times. The reproducibility of the results is satisfactory, characterized by differences lower than 20% among the individual devices, the short time stability (hours) is about 2% whereas the medium time stability (days/months) of the baseline resistance value is close to 5%.

Response to a reducing gas: CO.

The plots in Figure 11 show the response of the different materials to 500 ppm of CO in air and in nitrogen, respectively, as a function of temperature. From the discussion in the previous sections it is expected that the sensing mechanism can be mostly attributed to a direct bond of CO to the perovskite surface according to the following reaction [52]:

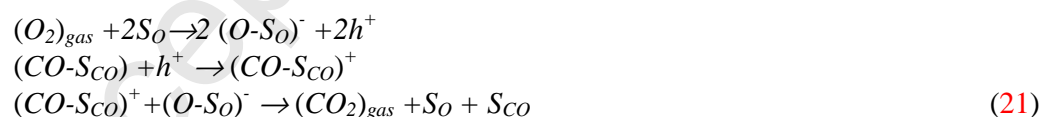


where S_{CO} indicates a surface adsorption site for CO and h^+ is a hole (hereafter S_X is a surface adsorption site for X). The reaction (20) is divided into two steps: adsorption of a neutral species and ionization of the adsorbate with the transfer of an electron to the material. **This electron can occupy a hole and subtract a carrier from the bulk. The charge localized at the surface modifies the electric field at the surface (irrespective of its sign) so as to increase the sensor resistance.** A large variation of conductivity in presence of CO in Ar was observed also for LaCoO₃ [46].

The results in Figure 11 confirm that the presence of oxygen doesn't affect much the response to CO, indicating that the reaction with ionized pre-adsorbed oxygen in air is not a relevant phenomenon, at least for the stoichiometric material. In general for YCoO_3 the response to CO in air is larger than the one in nitrogen at high temperatures, whereas at lower temperature the opposite is true. This can be related to the presence of different oxygen adsorbed species: molecular or not very reactive at lower temperatures, hence not relevant to the sensing mechanism, and ionized, e.g. O^- , above 250°C , relevant to the sensing mechanism, as it happens for the adsorption of other metal oxides [55]. Defective materials have in general a better response in nitrogen (where they present an increased response with respect to the stoichiometric material) than in air (where they have a response to CO comparable or worse with respect to the stoichiometric material). Doping with Pd increases the material response both in nitrogen and in air and, in general, also the response speed. On the other hand, Pt doped perovskites have a worse performance than those realized with the stoichiometric material. The different behavior of Pd doped perovskites with respect to Pt doped perovskites is probably due to the presence of PdO segregated on the surface or a reduced grain size (section 3.1.2 and [37]). Materials with Pt and Pd on the surface have a performance comparable or worse than the stoichiometric material.

Figure 11 about here

A further comment concerns the connection of the CO sensing capability of a material with its CO conversion catalytic activity. As already pointed out, there is a link between these two properties but no direct correspondence [15]. In particular, it is well known that the heterogeneous catalysis can be related to two types of adsorption: physisorption and chemisorption. Only in the latter type the adsorbate is strongly perturbed resulting in the sharing of electrons between the adsorbate and the adsorbent, and this is the mechanism relevant to gas sensing. Since it may require a very high temperature, and the materials under study are active as catalysts at a relatively low temperature (see figure 4), the catalytic oxidation of CO may be mostly related to physisorbed oxygen. Moreover, in terms of surface reactions involving chemisorbed species there could be at least two well known mechanisms related to catalysis (Langmuir-Hinshelwood and Rideal-Eley). In the first case a reaction involved both in catalysis and in sensing could be:



Whereas in the second case the reaction could be:



Only in reaction paths of the second type there is a clear beneficial effect of the pre-adsorbed oxygen on the magnitude of the sensor response to CO.

In fact in this case when working in air a certain amount of pre-adsorbed ionized oxygen will be present on the surface (first reaction in (22)), causing the baseline resistance value to be smaller than the one measured when operating in inert environment. As already discussed we recall that for the tested material this effect is absent or small (even for Pd doped materials where it can be

observed at high temperature). If some ionized oxygen is on the surface, when the CO gas is injected two effects contribute to the sensor response: the CO direct adsorption and ionization, responsible for a resistance increase also when working in N_2 (see reactions 20), and the removal of ionized atomic oxygen given by CO oxidation, which is supposed to free a trapped electron modifying the charge on the surface (as shown by the second reaction in (22)).

In reactions of the first type a lot of CO_2 can be produced with no net variation of the charge trapped on the surface.

The analysis of the transients confirms the above mentioned marginal contribution of oxygen in response to CO of these materials: the effect of the reaction in eq. (22) on the sensor response shows up only in a limited increase both in the extent and the speed of the response at high temperature. These comments apply in general for the tested materials, including those doped with Pd which show, as already mentioned, the most significant response to CO (Figure 12).

Figure 12 about here

As a last consideration, at the optimum temperatures for the response to CO the response to NO_x is quite small (as it will be shown later) and the one to CH_4 is negligible. The above considerations can be better understood analyzing the results reported in Figures 13-14, where the responses to the different test gases of a sample sensor of the best performing materials are shown. The lower plots in figures 13-14 show the response of these sensors at temperatures where the response to NO_x is small, whereas the response to CO is still close to its maximum value.

It can be noted that the CO response is highly correlated with the behavior of the qV_s assessed when analyzing the resistance baseline value in the same environment, with the exception of the Pt doped materials. It can be seen that the response to CO is larger if the potential barrier is higher, as expected from [41]. In the figures also typical sensor normalized resistance behaviors versus time at the optimum operating temperature are reported. In general, the developed materials show a modest response toward CO, when compared to some n-type metal oxides, nevertheless they operate fast, in fact it can be seen that complete recovery is obtained in some minutes. Note that responses to CH_4 are not reported, because no measurable response was recorded up to concentration of 10000 ppm in air.

Figure 13 about here

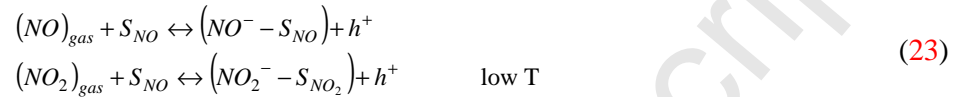
Figure 14 about here

Response to NO_x .

At temperatures lower than $200^\circ C$, where no appreciable response to CO is seen, a large response to NO_x is recorded: in this temperature range these two gases oxidize the sensor surface reversibly, as it can be seen in figures 15 and 16, and the response is fast. Actually, the response times depend not only on temperature but also on the target gas concentration, in particular the response time increases when concentration decreases.

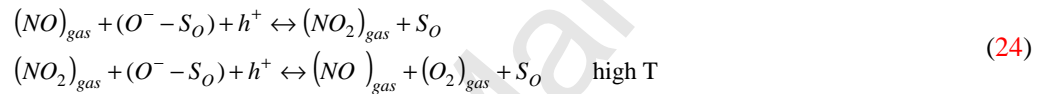
At higher temperatures the surface is reduced by both NO and NO_x, and a larger response is given by the same material that better responds also to CO. Nevertheless, the optimum temperature for the oxidation of NO_x is lower than the one of CO: above 300°C the response to NO_x can be neglected as can be seen in figure 15.

The observed data, see also the typical responses as a function of time shown in figure 16, can be explained by the simultaneous presence of two different chemical reactions: one implying the oxidation of the surface, which is faster and favored at low temperatures, the other one reducing the surface, which is slower and favored at higher temperatures. A similar behavior is seen for NO. From the literature the following possible routes can be assumed for gas reduction [56-59]:



As can it be seen the target gases oxidize the surface and lowers the resistance because adsorbed NO_x⁻ enhances the surface density of carriers. The largest response is seen around 180°C.

A possible route for the oxidation of the gas is [56-59]:



Related to these reactions an increase in the resistance is expected. This is a weaker effect, in fact a low amount of adsorbed oxygen on the grain surface is expected, as discussed above; only Pd doped sensors show an appreciable response related to this behavior between 200°C and 300°C.

In figure 16 the response in air are compared with those in nitrogen; from the reactions above it is expected that in the absence of oxygen there would be no reduction of the surface, being this latter a reaction which requires a pre-adsorbed ionized oxygen as a reagent. So the slow increase of the resistance during the gas injection phase, that above 200°C is present also in nitrogen (even if smaller than the one seen in air), can't be explained by the reactions (24). To explain this phenomenon another mechanism of resistance increase has to play a role: this could be, for instance, a re-equilibrium of the ionized intrinsic acceptor surface defects, that is related to injection of holes due to the gas reduction (eqs. 24). This seems to be the dominant mechanism from experimental observations especially for the stoichiometric material. A similar shape of the response is seen for an n-type material interacting with a reducing gas in the absence of oxygen [48].

The response to NO_x at low temperature where it behaves as an oxidizing gas is reduced by the presence of Pd, as expected, whereas it is enhanced in the defective material.

Figure 15 and Figure 16 about here

3.4.3 Effect of humidity

As in other perovskite materials the presence of humidity does not affect the conductivity in air very much [49]. Resistances measured in air and in humid air are very close and the difference results

smaller than measurement uncertainty. In the following figure (Figure 17) results obtained with $\text{YCo}_{1-x}\text{Pd}_x\text{O}_3$ are shown, it can be seen that both baseline resistance and gas response are not affected by the presence of humidity.

Figure 17 about here

Conclusions

In this work the preparation and the subsequent characterization of different toxic gas sensors based on yttrium cobalt perovskite (YCoO_3) are presented: the tested sensors are based on the stoichiometric material, on non-stoichiometric materials and on materials containing platinum or palladium.

Experimental results show that catalytic and sensor behavior strongly depend on composition and structure of the perovskite ceramic.

Pd doped materials show the best response to CO in the temperature range around 300°C , where the responses towards NO_x result very low. The improved response of these materials is mainly correlated with the presence of PdO segregated on the surface. A similar behavior was reported for LaCoO_3 [8] that shows a significant improvement of CO response with the addition of PdO. On the other hand, the responses of all the tested materials to NO_x are satisfactory at temperatures below 200°C , where the sensor surface is reversibly oxidized. The best results are found for defective powders (up to $\sim 2.5\%/ppm$ @ 12 ppm for NO_2 , and up to $\sim 1.8\%/ppm$ @ 12 ppm for NO) with fast response/recovery ($T_{\text{resp}}/T_{\text{rec}}$): for defective materials we have at 180°C $T_{\text{resp}} \sim 0.6$ min and $T_{\text{rec}} \leq 2$ min @ 12 ppm for both NO and NO_2). On the other hand, all the prepared sensors do not show an appreciable response to CH_4 at concentrations up to 10000 ppm, and, moreover, all these materials have proved to be insensitive to ambient humidity.

The tested materials show responses similar to the most perovskite sensors described in the literature [8]. The gas sensing properties of the different materials were discussed at the light of the different material compositions, structure and surface properties. It was shown that the materials that behave best as catalysts for CO conversion not always show the best performance as CO gas sensors. Low temperature CO conversion seems to be correlated to weakly adsorbed oxygen, whereas conductivity variations seem to be mostly related to a direct bond with the surface. Whereas the introduction of defects seems in general to improve the direct adsorption especially of oxidizing gases.

Acknowledgments

This work was partially supported by US ARMY RDECOM under the project “Perovskite Based Sensors Artificial Olfactory System (PSAOS)”

References

- [1] P. Ciambelli, S. Cimino, L. Lisi, M. Faticanti, G. Minelli, I. Pettiti, P. Porta, La, Ca and Fe oxide perovskites: preparation, characterization and catalytic properties for methane combustion, *Applied Catalysis B: Environmental*, 33, (2001), 193-203.
- [2] P. Porta, S. Cimino, S. De Rossi, M. Faticanti, G. Minelli, I. Pettiti, AFeO₃ (A=La, Nd, Sm) and LaFe_{1-x}Mg_xO₃ perovskites: structural and redox properties, *Materials Chemistry and Physics*, 71, (2001), 165-173.
- [3] V.M. Goldschmidt, *Geochemische Verteilungsgesetze der Elemente. VII. Die Gesetze der Kristallchemie. Skrifter Norske vidensk. Akad. Oslo, I: Mat. Natur.*, 2, (1926), 117-124.
- [4] P. Porta, S. De Rossi, M. Faticanti, G. Minelli, I. Pettiti, L. Lisi, M. Turco, Perovskite-Type Oxides: I. Structural, Magnetic, and Morphological Properties of LaMn_{1-x}Cu_xO₃ and LaCo_{1-x}Cu_xO₃ Solid Solutions with Large Surface Area, *J. Solid State Chem.*, 146, (1999), 291-304.
- [5] P. Salomonsson, T. Griffin, B. Kasemo, Oxygen desorption and oxidation-reduction kinetics with methane and carbon monoxide over perovskite type metal oxide catalysts, *Applied Catalysis A: General*, 104, (1993), 175-197.
- [6] Z. Zhong, K. Chen, Y. Ji, Q. Yan, Methane combustion over B-site partially substituted perovskite-type LaFeO₃ prepared by sol-gel method, *Applied Catalysis A: General*, 156, (1997), 29-41.
- [7] P. Ciambelli, S. Cimino, G. Lasorella, L. Lisi, S. De Rossi, M. Faticanti, G. Minelli, P. Porta, CO oxidation and methane combustion on LaAl_{1-x}Fe_xO₃ perovskite solid solutions, *Applied Catalysis B: Environmental*, 37, (2002), 231-241.
- [8] J. W. Fergus, Perovskite oxides for semiconductor-based gas sensors, *Sensors and Actuators B: Chemical*, 123, (2007), 1169-1179.
- [9] C. Doroftei, P.D. Popa, F. Iacomi, Synthesis of nanocrystalline La-Pb-Fe-O perovskite and methanol-sensing characteristics, *Sensors and Actuators B*, 161, (2012), 977-981.
- [10] L. Malavasi, C. Tealdi, G. Flor, G. Chiodelli, V. Cervetto, A. Montenero, M. Borella, NdCoO₃ perovskite as possible candidate for CO-sensors: thin films synthesis and sensing properties, *Sensors and Actuators B* 105, (2005), 407-411.
- [11] K. Fan, H. Qin, Z. Zhang, L. Sun, L. Sun, J. Hu, Gas sensing properties of nanocrystalline La_{0.75}Ba_{0.25}FeO₃ thick-film sensors, *Sensors and Actuators B*, 171-172, (2012), 302-308.
- [12] P. Song, Q. Wang, Z. Yang, CO-sensing characteristics of La_{0.8}Pb_{0.2}Fe_{0.8}Co_{0.2}O₃ perovskite films prepared by RF magnetron sputtering *Physica E* 41 (2009) 1479-1483.
- [13] C.M. Chiu, Y.H. Chang, The influence of microstructure and deposition methods on CO gas sensing properties of La_{0.8}Sr_{0.2}Co_{1-x}Ni_xO_{3-d} perovskite films, *Sensors and Actuators B*, 54, (1999), 236-242.

- [14] R.D. Shannon, Revised effective ionic radii and systematic studies of interatomic distances in halides and chalcogenides, *Acta Cryst. A*, 32, (1976), 751-767.
- [15] G. Korotcenkov, Metal oxides for solid-state gas sensors: what determines our choice?, *Materials Science and Engineering B*, 139, (2007), 1–23.
- [16] M. Hübner, N. Bârsan, U. Weimar, Influences of Al, Pd and Pt additives on the conduction mechanism as well as the surface and bulk properties of SnO₂ based polycrystalline thick film gas sensors, *Sensors and Actuators B: Chemical*, 171, (2012), 172-180.
- [17] M. Schweizer-Berberich, J.G. Zheng, U. Weimar, W. Göpel, N. Bârsan, E. Pentia, A. Tomescu, The effect of Pt and Pd surface doping on the response of nanocrystalline tin dioxide gas sensors to CO, *Sensors and Actuators B: Chemical*, 31(1–2), (1996), 71-75.
- [18] A.C. Larson, R.B. Von Dreele, General structure analysis system (GSAS), Los Alamos National Laboratory Report, LAUR 86-748 (2000).
- [19] B.H Toby, EXPGUI-A graphical user interface for GSAS, *J.Appl. Cryst.* 34, (2001), 210-213.
- [20] G. Caglioti, A. Paoletti, F.P. Ricci, Choice of collimators for a crystal spectrometer for neutron diffraction, *Nucl. Instruments*, 3, (1958), 223-228.
- [21] A. Beran, E. Libowitzky, T. Armbruster, A single-crystal infrared spectroscopic and X-ray diffraction study of untwinned San Benito perovskite containing OH groups, *Canadian Mineralogist* 34, (1996), 803-809.
- [22] G. Demazeau, M. Pouchard, P. Hagenmuller, Sur de nouveaux composés oxygénés du cobalt +III dérivés de la perovskite, *J. Solid State Chem.*, 9, (1974), 202-209.
- [23] A Mehta, R Berliner, RW Smith, The Structure of Yttrium Cobaltate from Neutron Diffraction, *J Solid State Chem.*, 130, (1997), 192-198.
- [24] O.S. Buassy-Monroy, C.C. Luhrs, A. Chavez-Chavez, C.R. Michel, Synthesis of crystalline YCoO₃ perovskite via sol-gel method. *Material Letters*, 58, (2004), 716-718.
- [25] K Knížek, Z. Jiráček, J. Hejtmánek, M. Veverka, M. Maryško, B.C. Hauback, H. Fjellvåg, Structure and physical properties of YCoO₃ at temperatures up to 1000 K, *Physical Review B*, 73, (2006), 214443, 6p.
- [26] G. Baldinozzi, J-F. Berar, G. Calvarin-Amiri, Rietveld refinement of two phase Zr-doped Y₂O₃, *Material Science Forum*, 278, (1998), 680-685.
- [27] X. Liu, C.T. Prewitt, High temperature X-ray diffraction study of Co₃O₄: transition from normal to disordered spinel, *Phys. Chem. Minerals*, 17, (1990), 168-172.
- [28] COD database, <http://www.crystallography.net/>9008478>

- [29] J. Waser, H.A. Levy, S.W. Peterson, The structure of PdO, *Acta Crystallographica*, 6, (1953) 661-663.
- [30] T. Addabbo, F. Bertocci, A. Fort, M. Mugnaini, V. Vignoli, L. Shahin, S. Rocchi, Versatile measurement system for the characterization of gas sensing materials, *Proc. of the 2013 IEEE International Instrumentation and Measurement Technology Conference*, (2013), 976-980.
- [31] Amador, C.J.D. Hetherington, E. Moran, M.A. Alario-Franco. Ba₂PrPtO₆: A novel double perovskite. *Journal of Solid State Chemistry* Volume 96, Issue 1, January 1992, Pages 132–140.
- [32] K. Ouchetto, F. Archaimbault, J. Choisnet, M. Et-Tabirou. New ordered and distorted perovskites: the mixed platinates Ln₂MPtO₆, (Ln = La, Pr, Nd, Sm, Eu, Gd; M = Mg, Co, Ni, Zn) . *Materials Chemistry and Physics* 51 (1997) 117-124.
- [33] Ikuya Yamada, Yuka Takahashi, Kenya Ohgushi, Norimasa Nishiyama, Ryoji Takahashi, Kohei Wada, Takehiro Kunimoto, Hiroaki Ohfuji, Yohei Kojima, Toru Inoue, and Tetsuo Irifune. CaCu₃Pt₄O₁₂: The First Perovskite with the B Site Fully Occupied by Pt⁴⁺. *Inorg. Chem.* 2010, 49, 6778–6780.
- [34] Mikiko Ochi, Ikuya Yamada, Kenya Ohgushi, Yoshihiro Kusano, Masaichiro Mizumaki, Ryoji Takahashi, Shunsuke Yagi, Norimasa Nishiyama, Toru Inoue, and Tetsuo Irifune. B-Site Deficiencies in A-site-Ordered Perovskite LaCu₃Pt_{3.75}O₁₂. *Inorg. Chem.* 2013, 52, 3985–3989.
- [35] Y. Nishihata, J. Mizuki, T. Akao, H. Tanaka, M. Uenishi, M. Kimura, T. Okamoto, N. Hamada, Self-regeneration of a Pd-perovskite catalyst for automotive emissions control, *Nature*, 418, (2002), 164-167.
- [36] S-J. Kim, S. Lemaux, G. Demazeau, J-Y. Kim, J-H. Choy, LaPdO₃: The First Pd^{III} Oxide with the Perovskite Structure, *J. Am. Chem. Soc.*, 123, (2001), 10413-10414.
- [37] G. L. Chiarello, J. D. Grunwaldt, D. Ferri, F. Krumeich, C. Oliva, L. Forni, A. Baiker, Flame-synthesized LaCoO₃-supported Pd: 1. Structure, thermal stability and reducibility, *Journal of Catalysis* 252, (2007), 127–136.
- [38] A. Eyssler, A. Winkler, O. Safonova, M. Nachtegaal, S.K. Matam, P. Hug, A. Weidenkaff, D. Ferri, On the State of Pd in Perovskite-Type Oxidation Catalysts of Composition A(B,Pd)O_{3±δ} (A = La, Y; B = Mn, Fe, Co), *Chem. Mater.*, 24, (2012), 1864-1875.
- [39] S. Sartipi, A. A. Khodadadi, Y. Mortazavi, Pd-doped LaCoO₃ regenerative catalyst for automotive emissions control, *Applied Catalysis B: Environmental*, 83(3-4), (2008), 214-220.
- [40] H. Liang, Y. Hong, C. Zhu, S. Li, Y. Chen, Z. Liu, D. Ye, Influence of partial Mn-substitution on surface oxygen species of LaCoO₃ catalysts, *Catalysis Today*, 201, (2013), 98–102.

- [41] A. Fort, M. Mugnaini, S. Rocchi, V. Vignoli, Surface state models for conductance response of metal oxide gas sensors during thermal transients, in *Chemical Sensors: Simulation and Modeling*, vol. 2: Conductometric-Type Sensors, G. Korotcenkov Ed., NJ: Momentum Press, (2012).
- [42] A. Fort, S. Rocchi, M. B. Serrano-Santos, R. Spinicci, V. Vignoli, Surface State Model for Conductance Responses During Thermal-Modulation of SnO Based Thick Film Sensors: Part I—Model Derivation, *IEEE Trans. on Instrum. and Meas.*, 55(6), (2006), 2107-2117.
- [43] A. Fort, M. Mugnaini, S. Rocchi, M. B. Serrano-Santos, R. Spinicci, V. Vignoli, Surface State Model for Conductance Responses During Thermal-Modulation of SnO₂-Based Thick Film Sensors: Part II—Experimental Verification, *IEEE Trans. on Instrum. and Meas.*, 55(6), (2006), 2107-2117.
- [44] A. Fort, M. Mugnaini, S. Rocchi, V. Vignoli, E. Comini, G. Faglia, A. Ponzoni, Metal-oxide nanowire sensors for CO detection: Characterization and modeling. *Sensors and Actuators B: Chemical*, 148(1), (2010), 283-291.
- [45] N. Bârsan, M. Hübner, U. Weimar, Conduction mechanisms in SnO₂ based polycrystalline thick film gas sensors exposed to CO and H₂ in different oxygen backgrounds, *Sensors and Actuators B: Chemical*, 157(2), (2011), 510-517.
- [46] L. Abadian, A. Malekzadeh, A. A., Khodadadi, M. Yadollah, Effects of Excess Cobalt Oxide Nanocrystallites on LaCoO₃ Catalyst on Lowering the Light off Temperature of CO and Hydrocarbons Oxidation, *Iran. J. Chem. Chem. Eng.*, 27(4), (2008), 71-77.
- [47] J.P. Dacquin, C. Dujardin, P. Granger, Catalytic decomposition of N₂O on supported Pd catalysts: Support and thermal ageing effects on the catalytic performances, *Catalysis Today*, 137(2), (2008), 390-396.
- [48] A. Fort, M. Mugnaini, S. Rocchi, M. B. Serrano-Santos, V. Vignoli, R. Spinicci, Simplified Models for SnO₂ Sensors during Chemical and Thermal Transients in Mixtures of Inert, Oxidizing and Reducing Gases, *Sensors and Actuators B: Chemical*, 124(1), 2007, 245-259.
- [49] G. Martinelli, M. C. Carotta, M. Ferroni, Y. Sadaoka, E. Traversa, Screen-printed perovskite-type thick films as gas sensors for environmental monitoring, *Sensors and Actuators B: Chemical*, 55(2), (1999), 99-110.
- [50] Z. Zhu, J. Guo, Y. Jia, X. Hu, Electronic structure and evolution of spin state in YCoO₃, *Physica B: Condensed Matter*, 405(1), (2010), 359-362.
- [51] Y. Liu, X.Y. Qin, Temperature dependence of electrical resistivity for Ca-doped perovskite-type Y_{1-x}Ca_xCoO₃ prepared by sol-gel process, *Journal of Physics and Chemistry of Solids*, 67(8), (2006), 1893-1898.
- [52] Y. Liu, H. Li, Y. Li, W. Sun, Effect of Sr substitution on electrical transport and thermoelectric properties of Y_{1-x}Sr_xCoO₃ (0 ≤ x ≤ 0.2) prepared by sol-gel process, *Ceramics International*, 39, (2013), 8189-8194.
- [53] Z. Zhou, Z. Tang, Z. Zhang, Studies on grain-boundary chemistry of perovskite ceramics as CO gas sensors, *Sensors and Actuators B: Chemical*, 93(1-3), (2003), 356-361.

- [54] N. P. Zaretskyi, L. I. Menshikov, A. A. Vasiliev, On the origin of sensing properties of the nanostructured layers of semiconducting metal oxide materials, *Sensors and Actuators B: Chemical*, 170, (2012), 148-157.
- [55] N. Barsan, U. Weimar, Conduction model of metal oxide gas sensors, *Journal of Electroceramics*, 7 (3), (2001), 143–167.
- [56] A. Fort, T. Addabbo, V. Vignoli, F. Bertocci, M. Mugnaini, A. Atrei, M. Gregorkiewitz, Gas-sensing properties and modeling of silver doped potassium hollandite, *Sensors and Actuators, B: Chemical*, 194, (2014), 427–439.
- [57] P.L. Martin, A.P. Quoc, R.S. Glass, Effect of Cr_2O_3 electrode morphology on the nitric oxide response of a stabilized zirconia sensor, *Sensors and Actuators B: Chemical*, 96 (1), (2003), 53–60.
- [58] A. Afzal, N. Cioffi, L. Sabbatini, L. Torsi, NO_x sensors based on semiconducting metal oxide nanostructures: progress and perspectives, *Sensors and Actuators B: Chemical*, 171, (2012) 25–42.
- [59] K. Wetchakun, T. Samerjai, N. Tamaekong, C. Liewhiran, C. Siriwong, V. Kruefu, A. Wisitsoraat, A. Tuantranont, S. Phanichphant, Semiconducting metal oxides as sensors for environmentally hazardous gases, *Sensors and Actuators B: Chemical*, 160 (1), (2011) 580–591.

Tables**Caption list**

Table I. Phase composition and crystallinity parameters of representative products as obtained from X-ray powder diffraction. Values with estimated standard deviations (in parentheses and referring to the last digits) were obtained from Rietveld refinement (for reliability indices see Table II). See text for explanations.

Table II. Unit cell volumes, site occupation factors *SOF* and average interatomic distances (pm) obtained from Rietveld refinement for a representative selection of the perovskite structures synthesized in this study. The reliability of refinement is indicated by the reduced chi-square χ^2 , the intensity weighted Bragg residual for the sole perovskite phase $R(F^2)$, and the overall powder residual R_p . CuK α radiation ($\lambda = 154.098$ pm), space group *Pbnm* §*Pnma*§, $T = 295$ K.

Accepted Manuscript

sample	batch		mass fraction (%)					peak width (cdeg)	
	x	#	perov.	yttria	spinel	Pd	PdO	X	Y
LaCoO ₃		La3	98	-	2	-	-	~16 ¹	-
		La4	99	-	1	-	-	~16 ¹	-
		LaB	99.5	-	.5	-	-	~16 ¹	-
YCoO ₃		1	77.8(1)	9.0(2)	13.2(3)	-	-	0.6(7)	23(2)
		2	83.4(1)	7.6(2)	9.0(3)	-	-	0.8(5)	18(2)
		3	96.5(1)	0.4(1)	3.1(1)	-	-	2.3(1)	9.4(2)
		4	95.0(1)	0.30(4)	4.7(1)	-	-	2.2(1)	10.4(2)
(Y,□)CoO ₃		32	93	1	6	-	-	~16 ¹	-
		34	94	1	5	-	-	~16 ¹	-
Y(Co,□)O ₃		10	96	4	0	-	-	~15 ¹	-
		30	90	8	2	-	-	~15 ¹	-
		31	93	7	0	-	-	~15 ¹	-
		S8	94	5	1	-	-	~10 ¹	-
		F63	93.6(2)	1.4(1)	5.0(2)	-	-	2.4(2)	9.1(4)
		S9	88	12	0	-	-	~10 ¹	-
Y(Co _{1-x} Pd _x)O ₃	0.1	12	92.4(2)	2.3(1)	2.7(6)	1.5(1)	1.1(1)	3.7(1)	11.5(4)
	“	S10	88	10	0	2	0	~10 ¹	-
	.07	13	94	1	4	1	0	~16 ¹	-
	.05	16	85	8	6	1	0	~15 ¹	-
	“	28	82.7(6)	7.9(2)	8.1(3)	0.64(6)	0.63(9)	3.9(2)	8.3(4)
	“	S11	95	5	0	0	0	~8 ¹	-
	“	S12	98	1	1	0	0	~10 ¹	-
	.03	14	94	3	2	0.5	0	~16 ¹	-
Y(Co _{1-x} Pt _x)O ₃	0.05	33	98.61(4)	0.9(1)	0.5(1)	-	-	~2 ²	26 ²
YCoO ₃ + Pd	0.02	11	95	2	3	0	0	~15 ¹	-
		27	81	9	10	0	<1	~15 ¹	-

1- estimated *FWHM* at $2\theta=27^\circ$, not corrected for instrumental broadening as are X and Y.

2- equivalent isotropic values.

Table I. Phase composition and crystallinity parameters of representative products as obtained from X-ray powder diffraction. Values with estimated standard deviations (in parentheses and referring to the last digits) were obtained from Rietveld refinement (for reliability indices see Table II). See text for explanations.

Accepted Manuscript

sample	#	unit cell	SOF		interatomic distances		fit criteria		
		V (Å ³)	Co	Y	Co-O (6)	Y-O (8)	R(F ²)	χ ²	Rp
LaCoO ₃	*	223.9(1)	1	1	193.2	271(22)	-	-	0.079
YCoO ₃	1	205.72(4)			-	-	0.037	1.54	0.095
	2	205.39(3)			-	-	0.040	1.55	0.094
	3	205.490(3)	0.947(9)	0.954(8)	193.3(1.2)	238(13)	0.027	1.97	0.060
	4	205.474(4)	0.958(9)	0.963(8)	193.7(1.7)	238(14)	0.029	2.00	0.062
Y(Co,□)O ₃	F63	205.375(6)	0.98(2)	0.97(2)	193.5(1.2)	238(15)	0.055	1.24	0.104
Y(Co _{0.9} Pd _{0.1})O ₃	12	205.455(3)	1.02(1)	1.01(1)	193.6(1.2)	238(15)	0.04	2.43	0.087
Y(Co _{0.95} Pd _{0.05})O ₃	28	205.601(8)	1.03(2)	1.00(2)	193.4(1.5)	237(15)	0.054	1.29	0.106
Y(Co _{0.95} Pt _{0.05})O ₃	33	207.74(2)	1.15(2)	1.02(2)	194.4(1.3)	238(14)	0.057	1.19	0.112

* values from Thornton et al [31], volume adapted to account for a unit cell containing 4 formula units, La for Y, and coordination number $CN(\text{La})=12$. The space group of LaCoO₃ is R-3c with Z=2 for the rhombohedral setting.

Table II. Unit cell volumes, site occupation factors *SOF* and average interatomic distances (pm) obtained from Rietveld refinement for a representative selection of the perovskite structures synthesized in this study. The reliability of refinement is indicated by the reduced chi-square χ², the intensity weighted Bragg residual for the sole perovskite phase $R(F^2)$, and the overall powder residual Rp. CuKα radiation (λ = 154.098 pm), space group *Pbnm* §*Pnma*§, *T* = 295 K.

Caption List

- Figure 1** Sensor structure: (a) heater; (b₁) temperature sensor, (b₂) chemical sensor.
- Figure 2** Calculated (line), observed (dots) and difference (below) X-ray powder diffraction pattern for sample #3, as obtained after Rietveld refinement. Ticks give, from bottom to top, reflection positions for YCoO₃, Y₂O₃ and Co₃O₄. CuK α radiation.
- Figure 3** SEM images of the perovskite-based sensing films: (a), (b) perovskite powders at different magnifications; (c) perovskite sensing film on the substrate.
- Figure 4** Catalytic activity of the prepared perovskite powders in CO oxidation.
- Figure 5** O₂ TPD of different perovskite materials derived from YCoO₃.
- Figure 6** H₂ TPR results for different YCoO₃ perovskite materials.
- Figure 7** (a1), (a2): baseline value of resistance (R_0) in synthetic air for different materials. (b1), (b2): potential barrier heights (qV_s), estimated for the same materials from the slopes of the log (R) versus 1/T curves.
- Figure 8** (a1), (a2): baseline value of resistance (R_0) for different materials. Red dashed lines: nitrogen; blue solid lines: air.
- Figure 9** Upper plots: charge density in the grain for a material similar to those proposed in this work. 'Large grain' ($R_g \gg \lambda_D$) case (a) and 'small grain' case (b). Lower plots: gray-level coded charge density for different values of N_s . 'Large grain' ($R_g \gg \lambda_D$) case (c1)-(c4) and 'small grain' case (d1)-(d4). The parameters for the numerical calculation are taken from [47].
- Figure 10** Upper plots: surface potential barrier for a material similar to those proposed in this work. 'Large grain' ($R_g \gg \lambda_D$) case (a1) and 'small grain' case (a2). Lower plots: normalized conductance. 'Large grain' ($R_g \gg \lambda_D$) case (b1) and 'small grain' case (b2). Red lines: fully depleted layer approximation. Blue lines: proposed model.
- Figure 11** (a1), (a2): responses of different materials to a mixture of CO (500 ppm) and air or nitrogen as a function of temperature. Sensor exposure time to CO is 4 minutes. Total flow is 200 mL/min.
- Figure 12** Sensor responses to CO in Air (blue lines) and N₂ (red lines) versus time @ T= 300 °C for: (a) YCoO₃; (b) YCo_{0.91}Pd_{0.09}O₃. Sensor exposure time to target gas is 4 minutes. Total flow is 200 mL/min. CO concentrations from left to right are: 1000, 500 and 250 ppm, respectively.
- Figure 13** YCoO₃: (a) sensor responses to CO and NO_x versus temperature (carrier gas: air; target gas concentrations listed in the legend); (b) sensor responses to CO and NO_x versus target gas concentration at the optimum temperature for CO detection (temperature shown in the legend); (c) sensor **resistance** versus time.

- Figure 14** $\text{YCo}_{0.91}\text{Pd}_{0.09}\text{O}_3$: (a) sensor responses to CO and NO_x versus temperature (carrier gas: air; target gas concentrations listed in the legend); (b) sensor responses to CO and NO_x versus target gas concentration at the optimum temperature for CO detection (temperature shown in the legend); (c) sensor **resistance** versus time.
- Figure 15** (a1), (a2): responses of different materials to a mixture of air and CO (500 ppm – blue lines) or air and NO_2 (24 ppm – black lines) as a function of temperature. Sensor exposure time to target gas is 4 minutes. Total flow is 200 mL/min.
- Figure 16** Response of the tested materials to NO_x . (a), (b): $\text{Y}_{1.1}\text{CoO}_3$ sensor responses versus time for different temperatures (between 160°C and 280°C) and for different carrier gases (air or nitrogen) to different NO_2 and NO concentrations, respectively; (c): response of the tested materials versus NO_x concentration at the optimum temperature (that is, the temperature where the response is maximum); (d), (e): responses of the tested materials as a function of temperature to a mixture of air/nitrogen and 12 ppm of NO and NO_2 , respectively. Sensor exposure time to target gas is 4 minutes. Total flow is 200 mL/min.
- Figure 17** Upper plots: baseline resistance of $\text{YCo}_{0.91}\text{Pd}_{0.09}\text{O}_3$ (a1) and YCoO_3 (a2). Lower plots: estimated activation energy, in air and humid air (37% RH @ 25°C) for $\text{YCo}_{0.91}\text{Pd}_{0.09}\text{O}_3$ (b1) and YCoO_3 (b2).

Figures

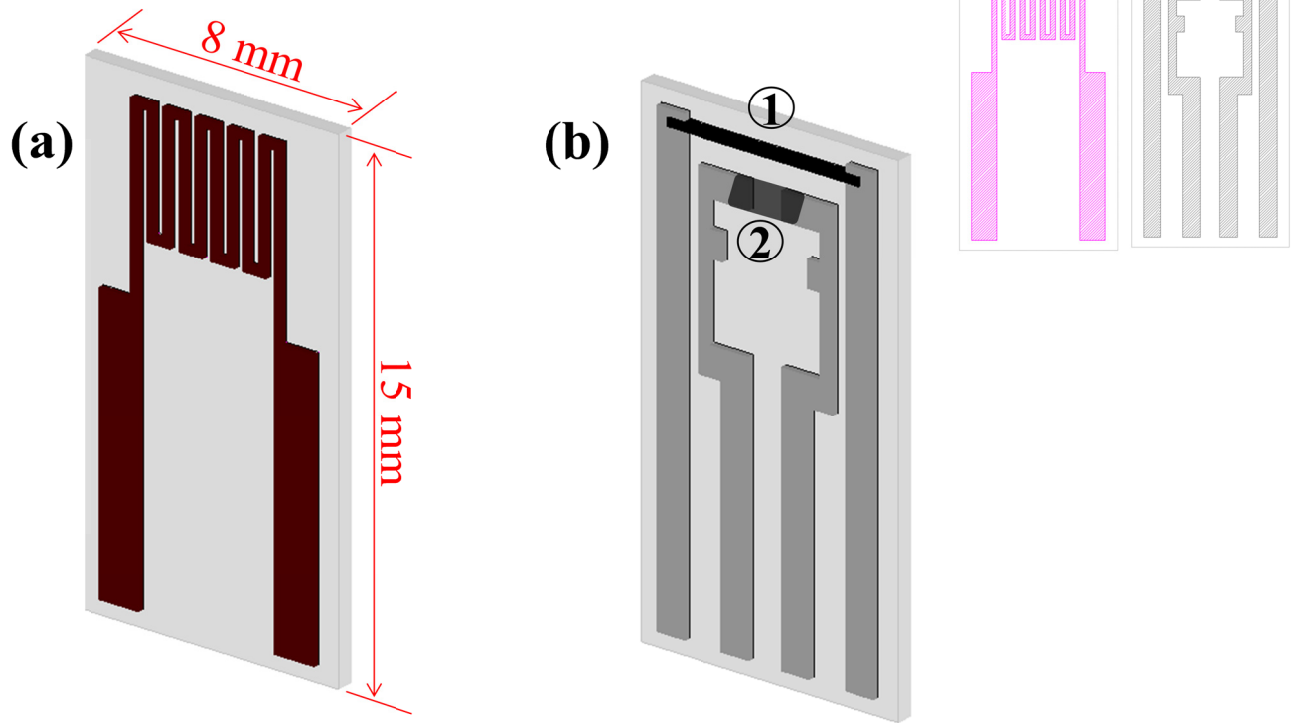


Figure 1. Sensor structure: (a) heater; (b₁) temperature sensor, (b₂) chemical sensor.

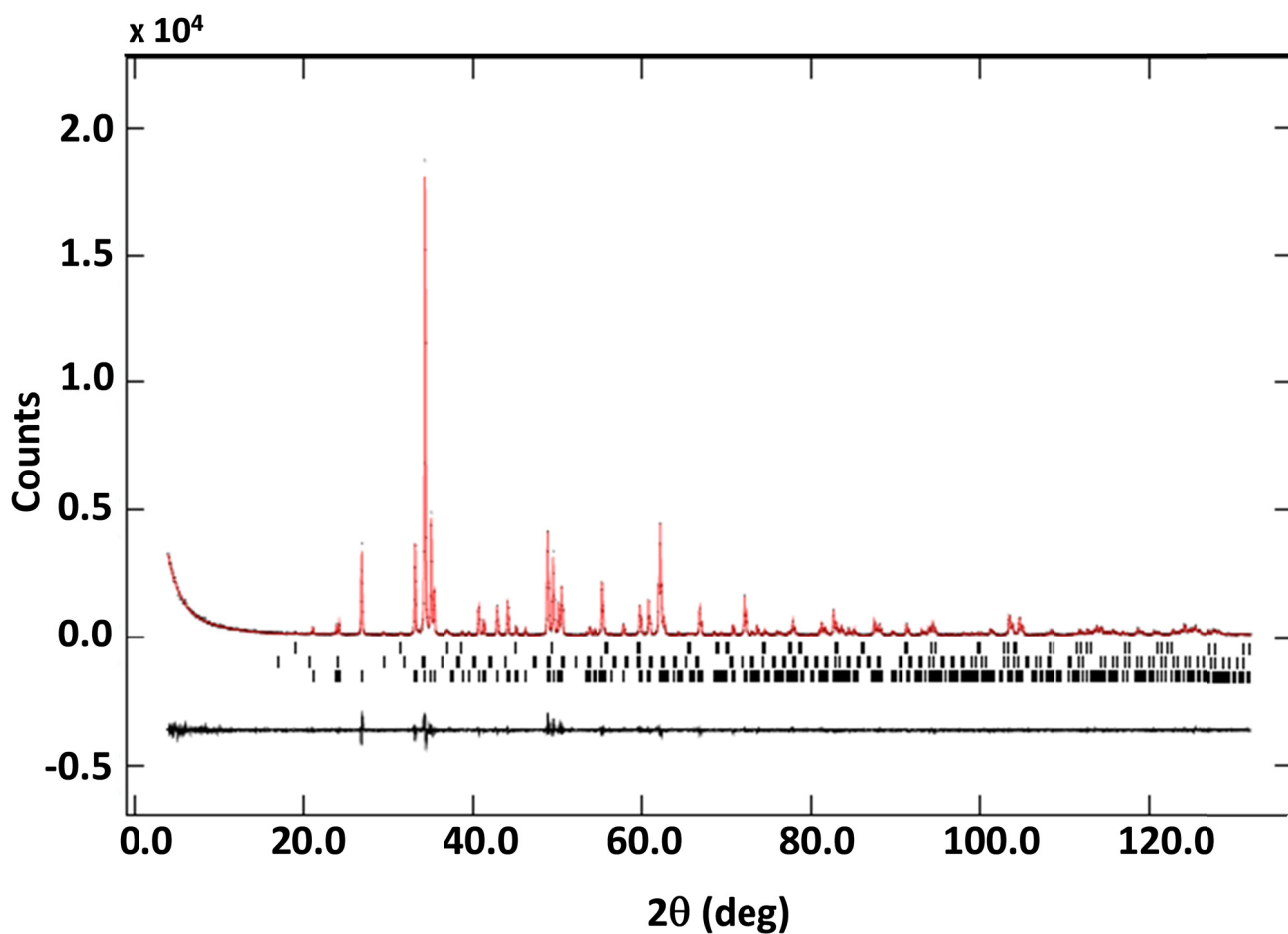


Figure 2. Calculated (line), observed (dots) and difference (below) X-ray powder diffraction pattern for sample #3, as obtained after Rietveld refinement. Ticks give, from bottom to top, reflection positions for YCoO_3 , Y_2O_3 and Co_3O_4 . $\text{CuK}\alpha$ radiation.

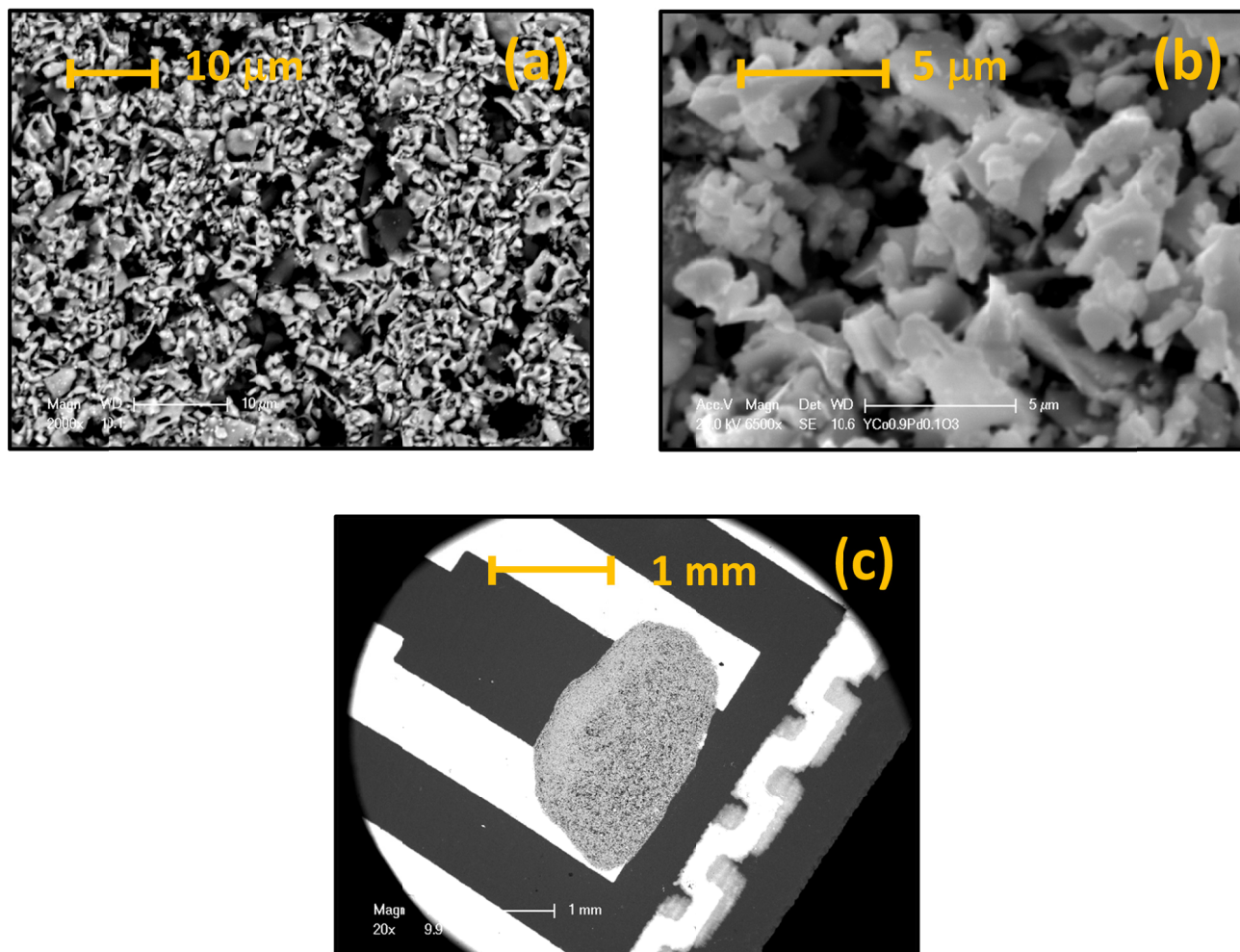


Figure 3. SEM images of the perovskite-based sensing films: (a), (b) perovskite powders at different magnifications; (c) perovskite sensing film on the substrate.

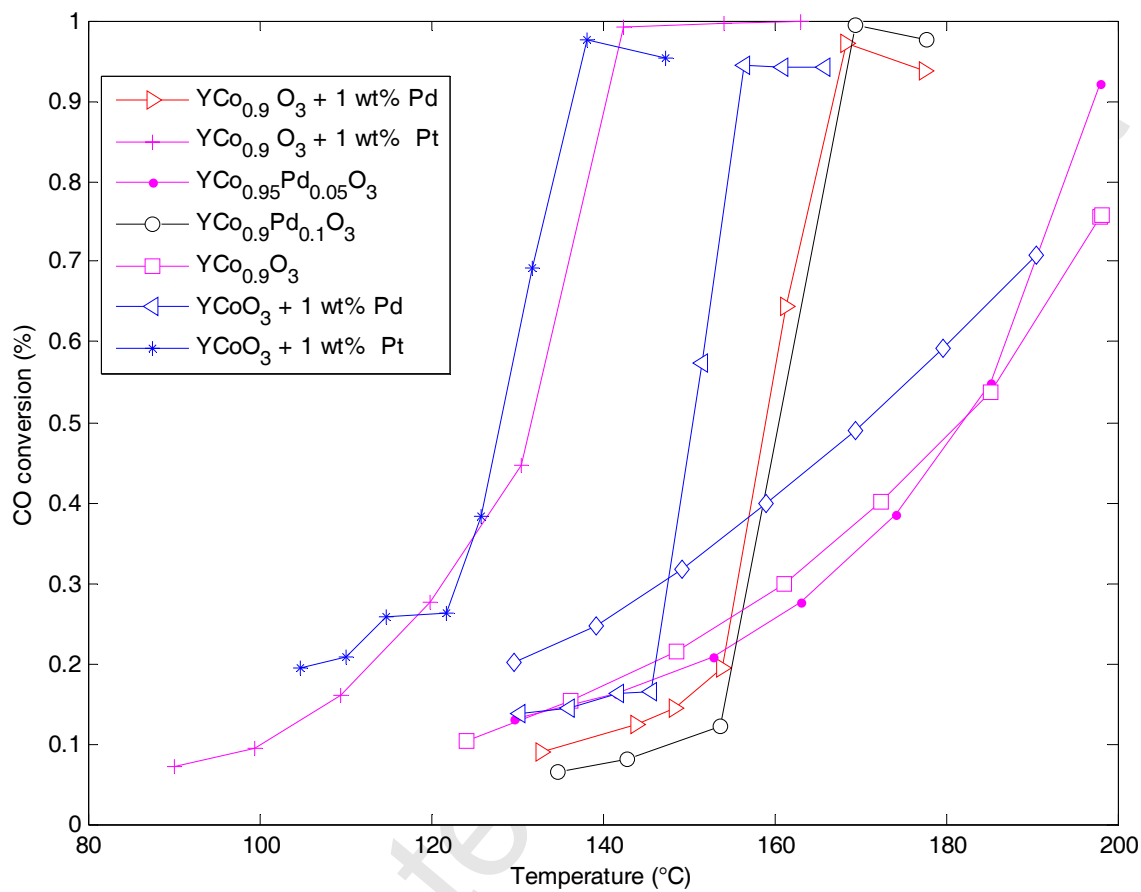


Figure 4. Catalytic activity of the prepared perovskite powders in CO oxidation.

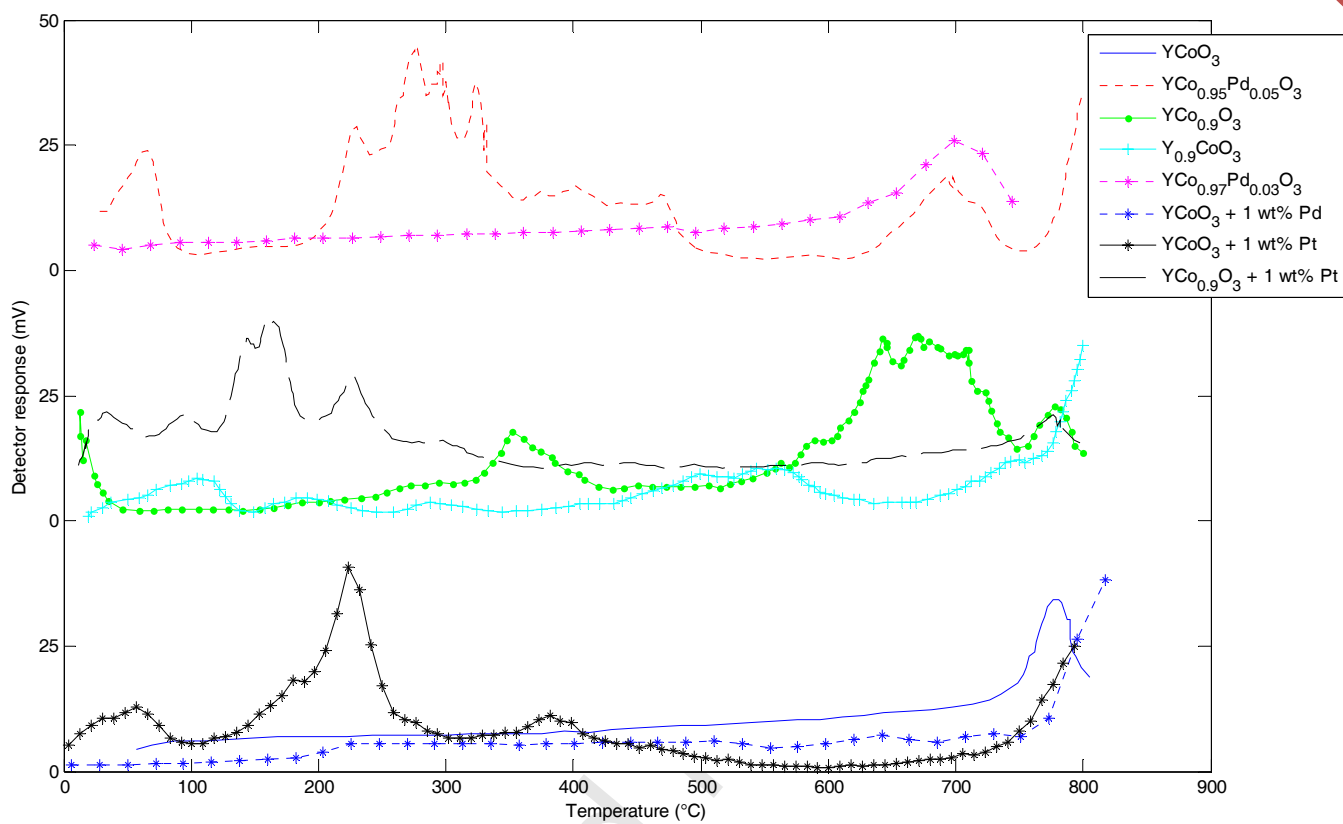


Figure 5. O₂ TPD of different perovskite materials derived from YCoO₃.

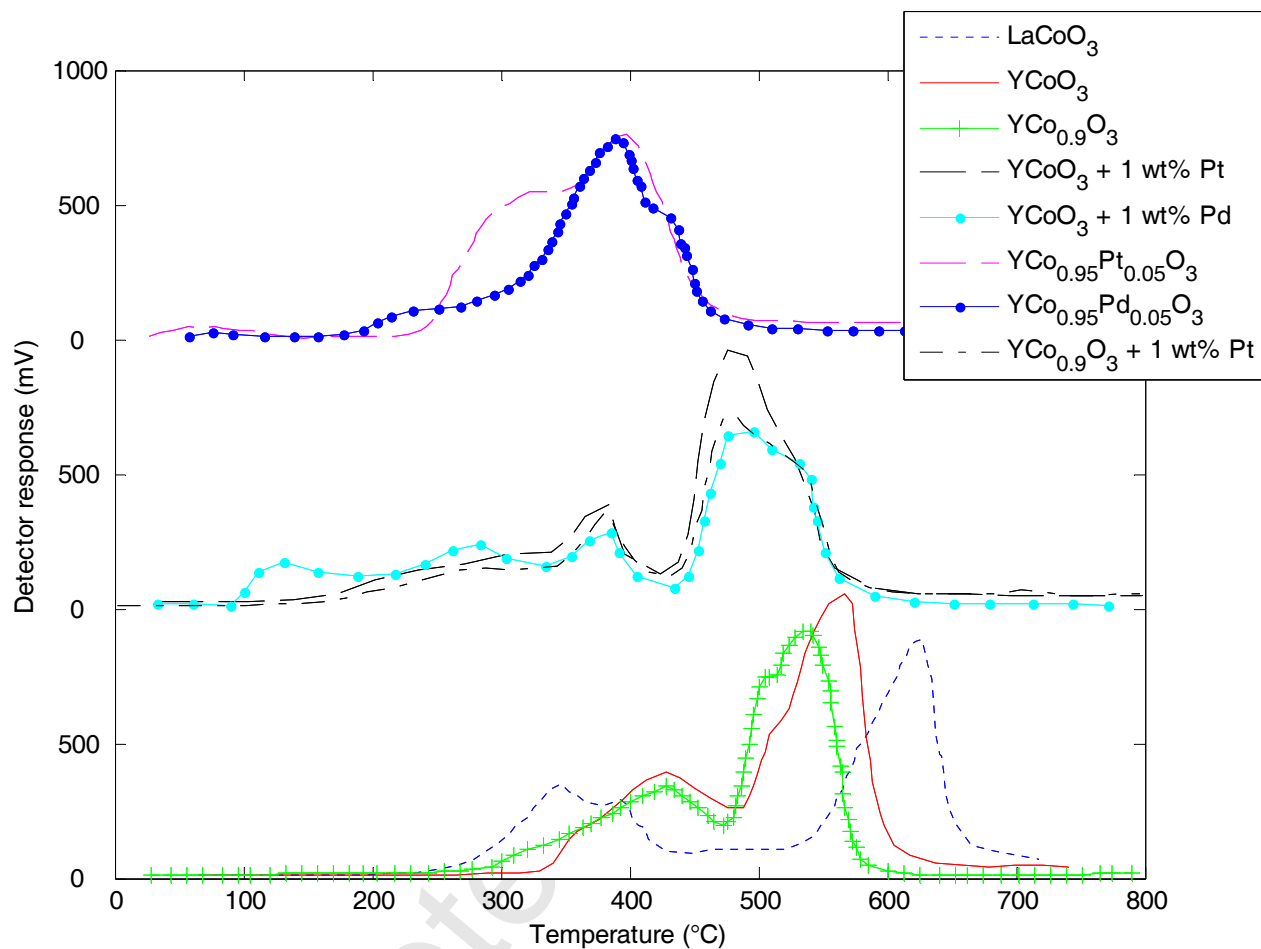


Figure 6. H₂ TPR results for different YCoO₃ perovskite materials.

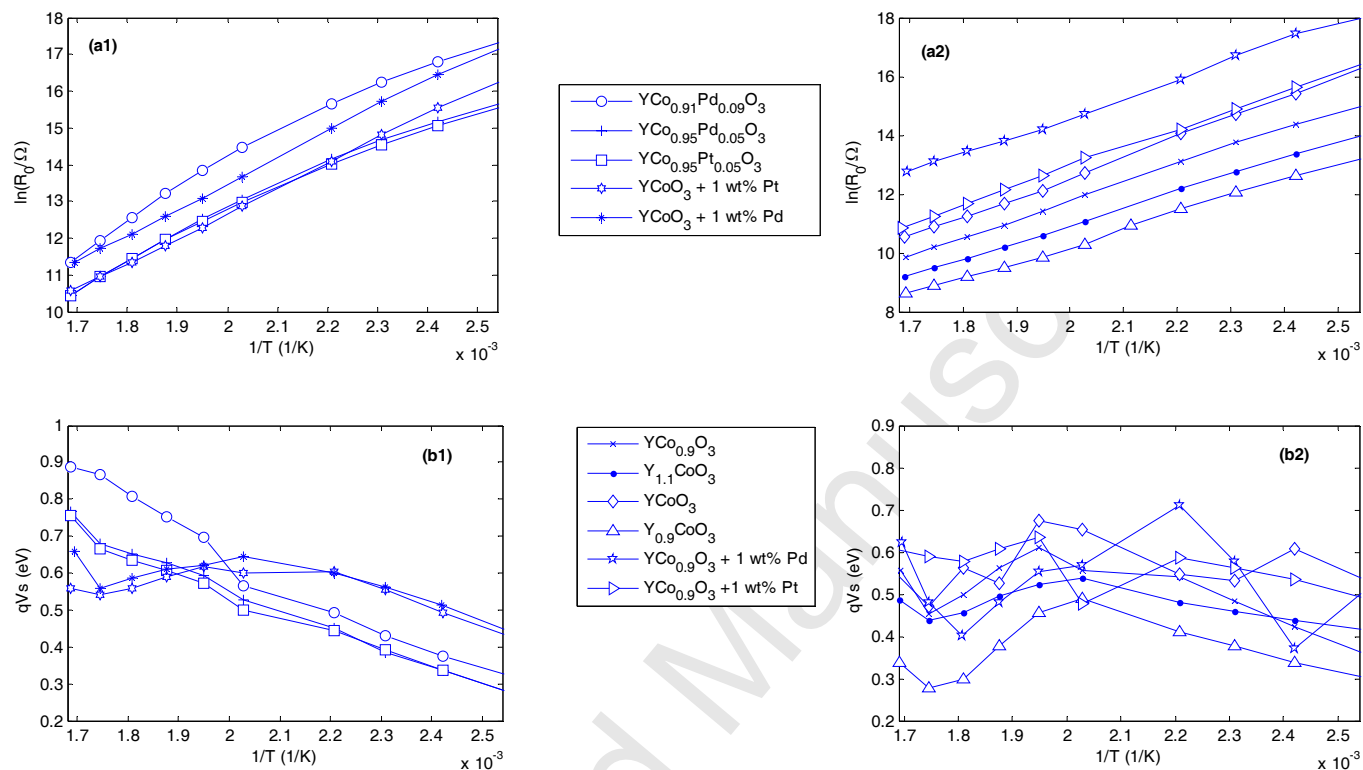


Figure 7. (a1), (a2): baseline value of resistance (R_0) in synthetic air for different materials. (b1), (b2): potential barrier heights (qV_s), estimated for the same materials from the slopes of the log (R) versus $1/T$ curves.

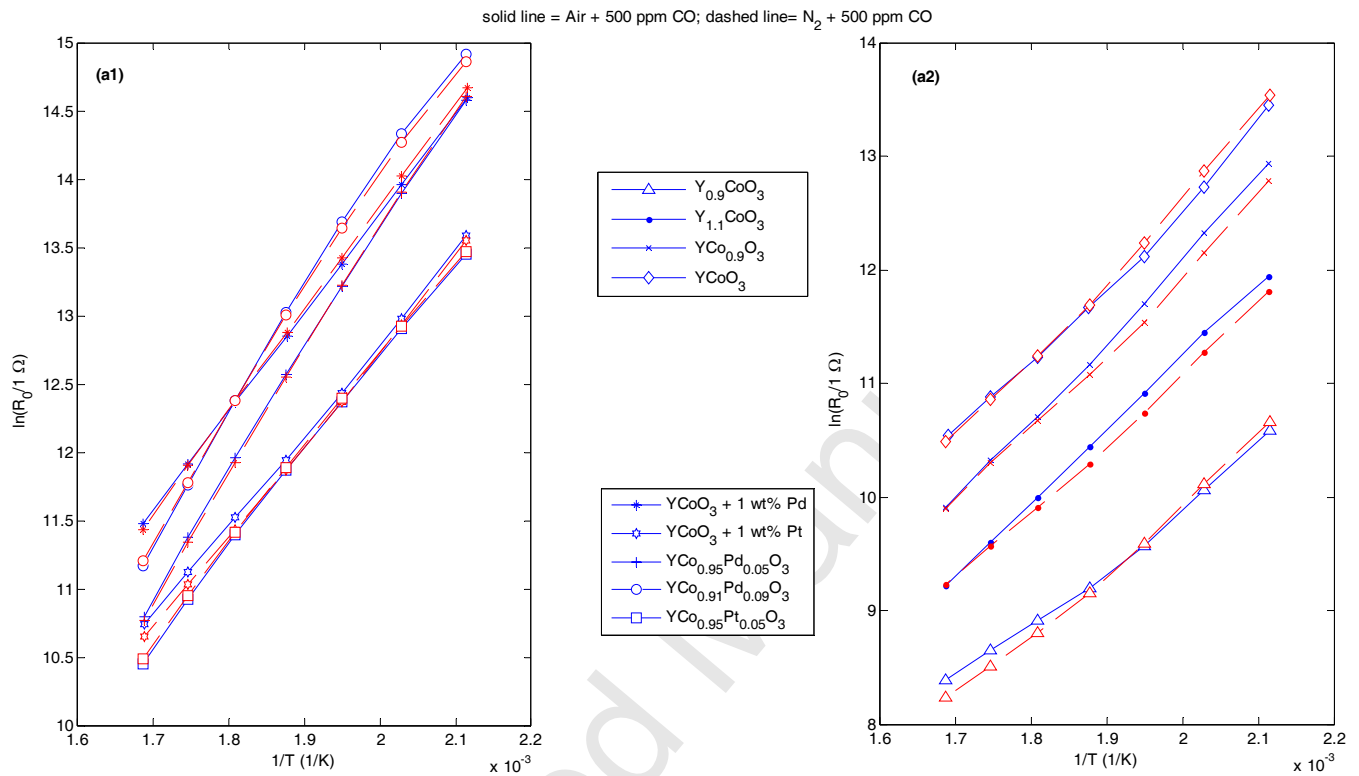


Figure 8. (a1), (a2): baseline value of resistance (R_0) for different materials. Red dashed lines: nitrogen; blue solid lines: air.

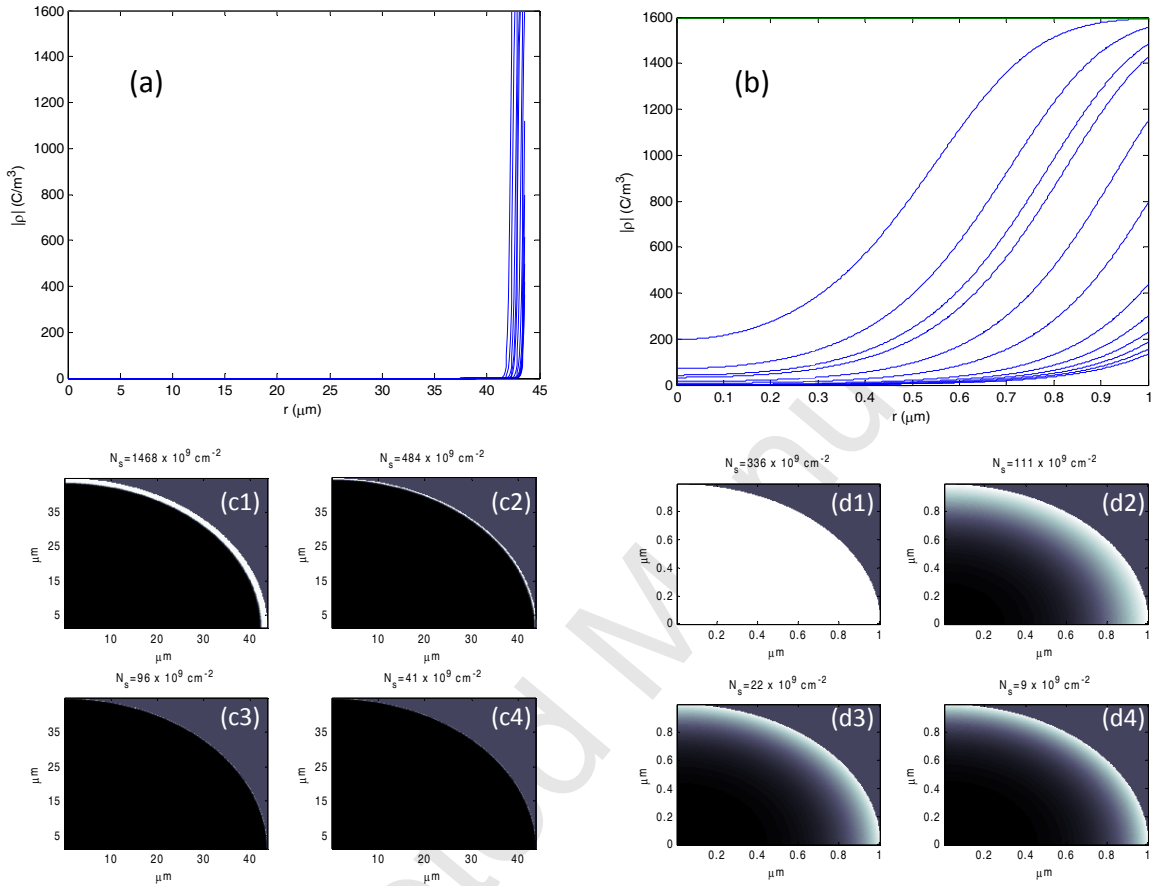


Figure 9. Upper plots: charge density in the grain for a material similar to those proposed in this work. 'Large grain' ($R_g \gg \lambda_D$) case (a) and 'small grain' case (b). Lower plots: gray-level coded charge density for different values of N_s . 'Large grain' ($R_g \gg \lambda_D$) case (c1)-(c4) and 'small grain' case (d1)-(d4). The parameters for the numerical calculation are taken from [47].

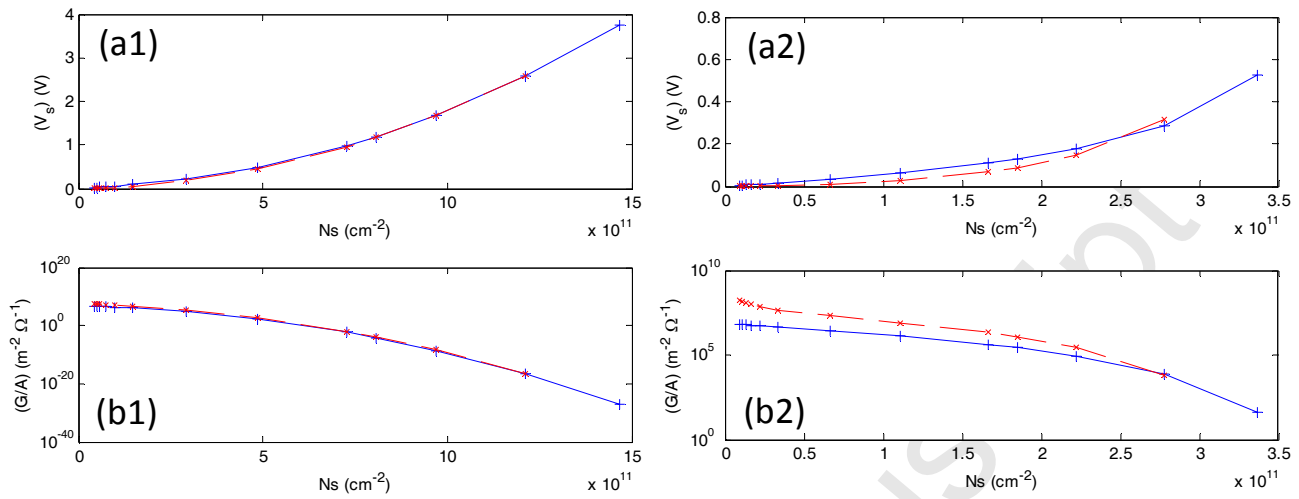


Figure 10. Upper plots: surface potential barrier for a material similar to those proposed in this work. 'Large grain' ($R_g \gg \lambda_D$) case (a1) and 'small grain' case (a2). Lower plots: normalized conductance. 'Large grain' ($R_g \gg \lambda_D$) case (b1) and 'small grain' case (b2). Red lines: fully depleted layer approximation. Blue lines: proposed model.

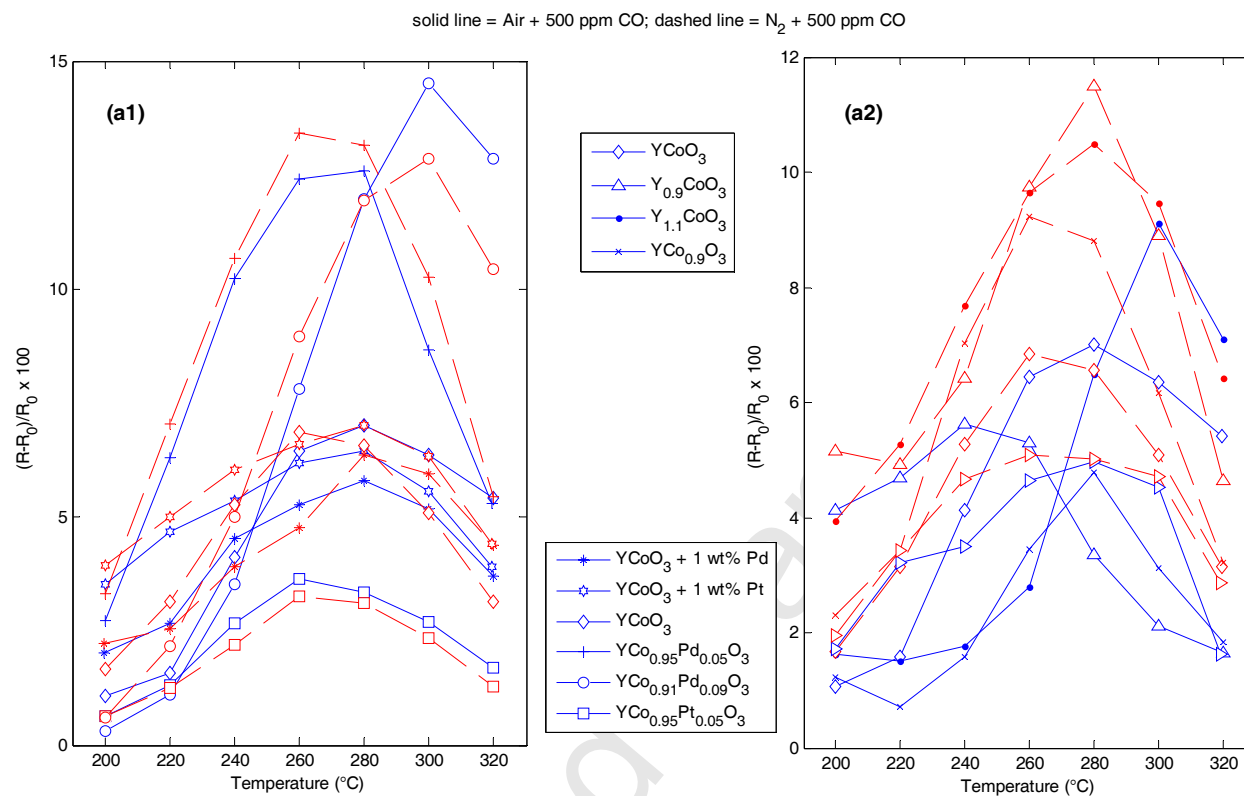


Figure 11. (a1), (a2): responses of different materials to a mixture of CO (500 ppm) and air or nitrogen as a function of temperature. Sensor exposure time to CO is 4 minutes. Total flow is 200 mL/min.

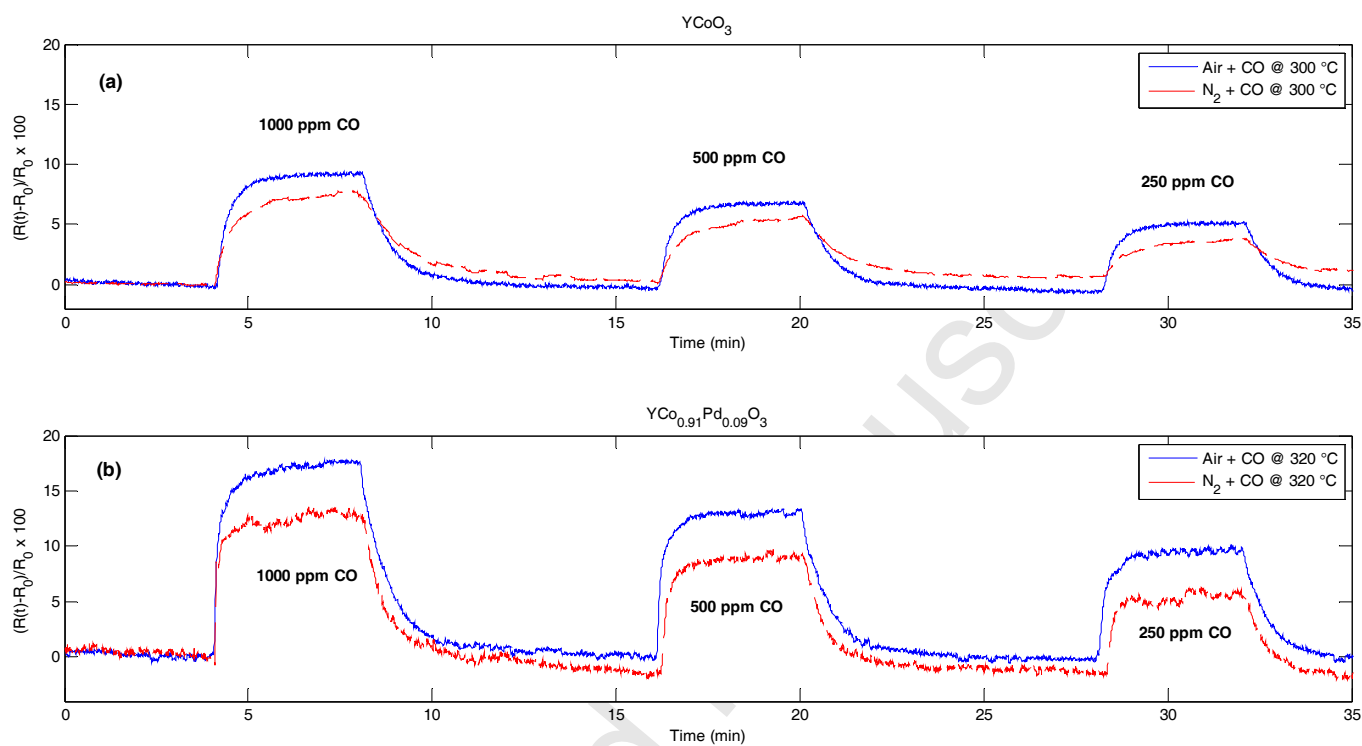


Figure 12. Sensor responses to CO in Air (blue lines) and N_2 (red lines) versus time @ $T=300\text{ }^\circ\text{C}$ for: (a) $YCoO_3$; (b) $YCo_{0.91}Pd_{0.09}O_3$. Sensor exposure time to target gas is 4 minutes. Total flow is 200 mL/min. CO concentrations from left to right are: 1000, 500 and 250 ppm, respectively.

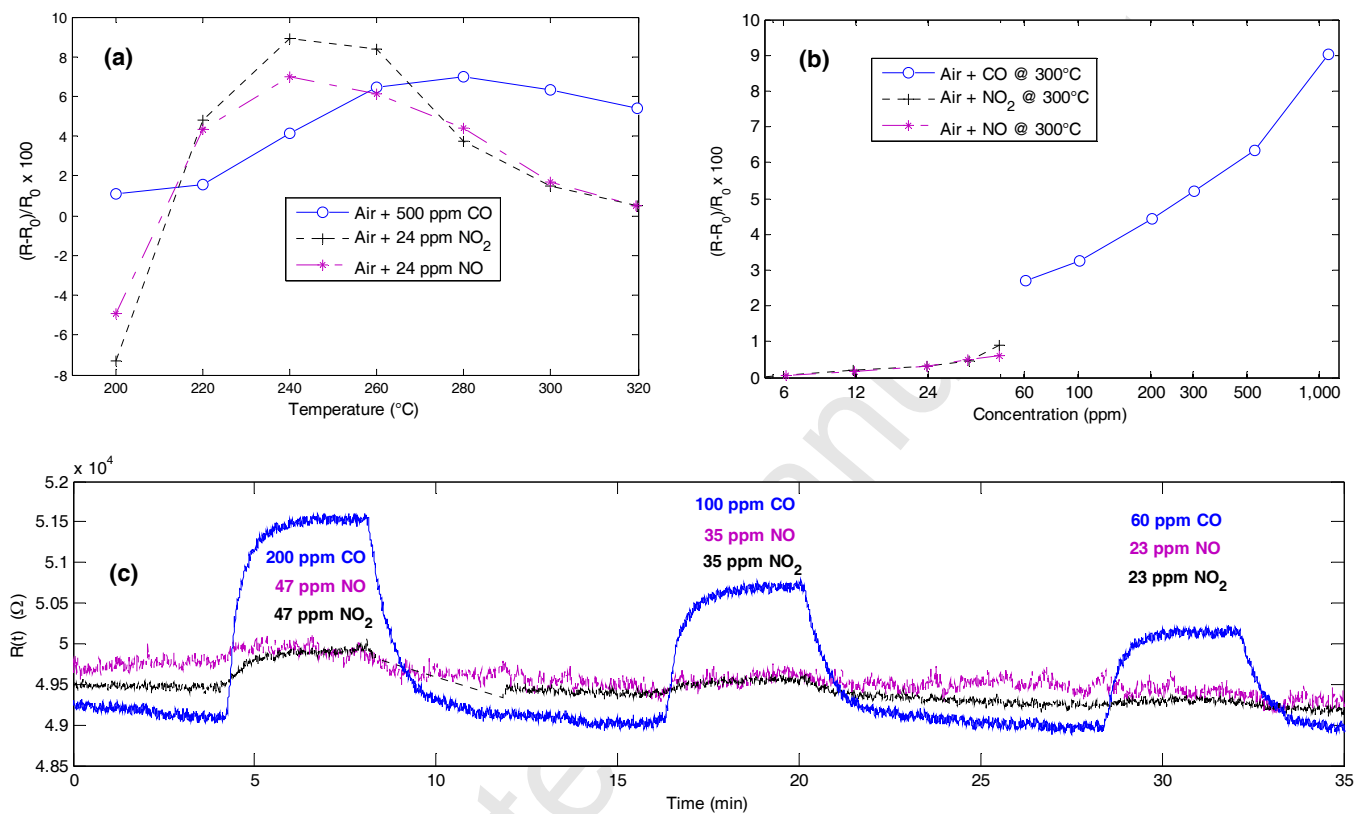


Figure 13. YCoO₃: (a) sensor responses to CO and NO_x versus temperature (carrier gas: air; target gas concentrations listed in the legend); (b) sensor responses to CO and NO_x versus target gas concentration at the optimum temperature for CO detection (temperature shown in the legend); (c) sensor resistance versus time.

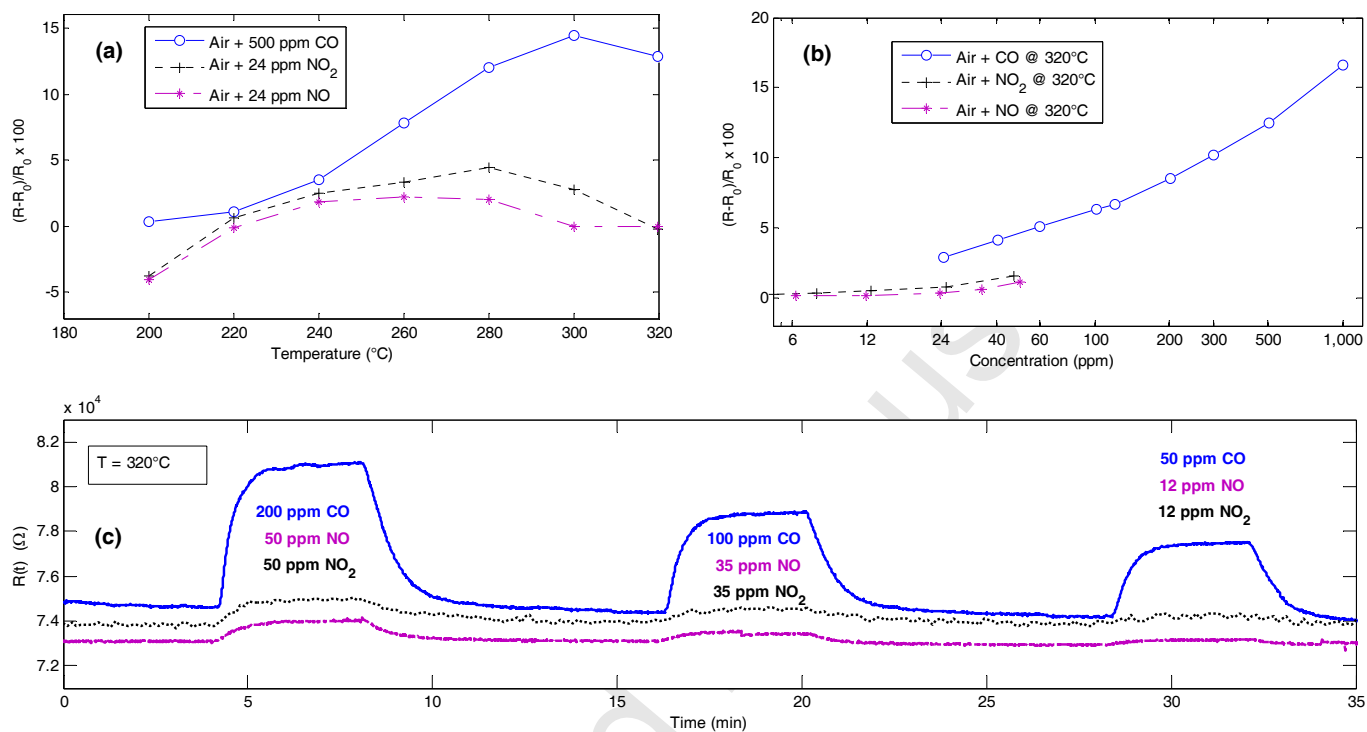


Figure 14. $\text{YCo}_{0.91}\text{Pd}_{0.09}\text{O}_3$: (a) sensor responses to CO and NO_x versus temperature (carrier gas: air; target gas concentrations listed in the legend); (b) sensor responses to CO and NO_x versus target gas concentration at the optimum temperature for CO detection (temperature shown in the legend); (c) sensor resistance versus time.

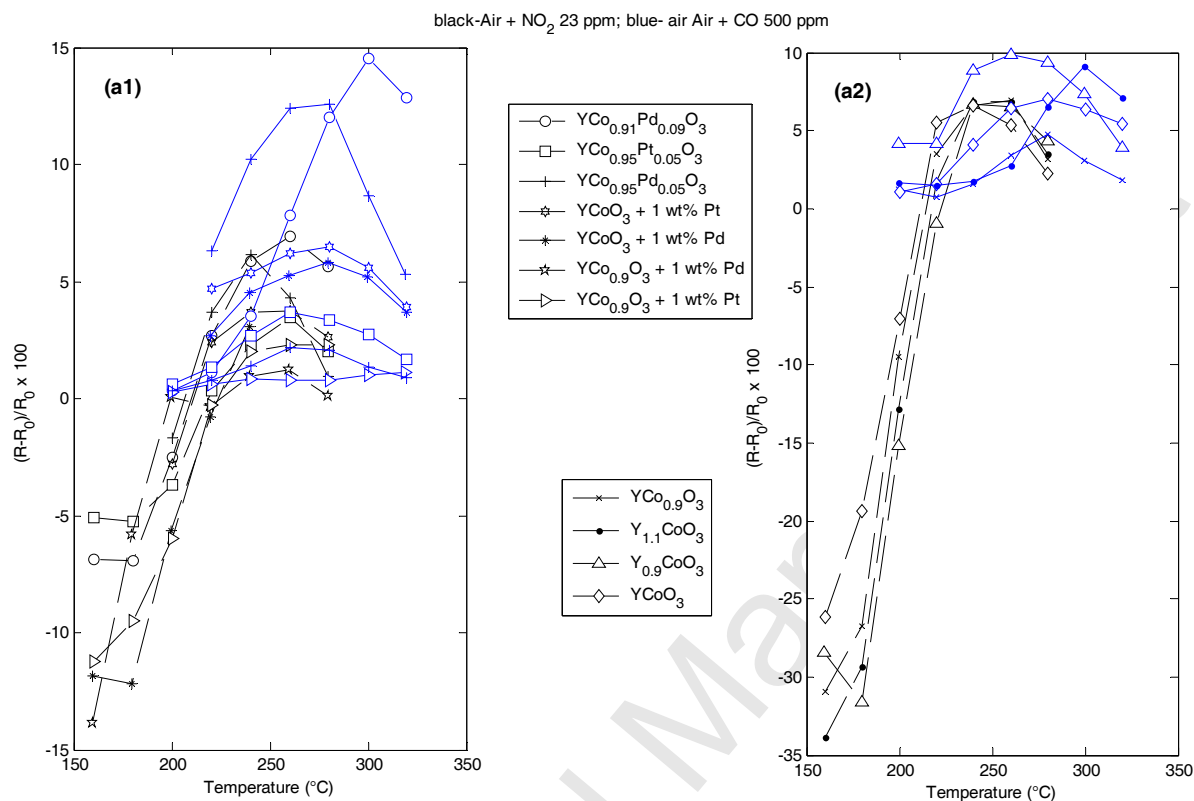


Figure 15. (a1), (a2): responses of different materials to a mixture of air and CO (500 ppm – blue lines) or air and NO₂ (24 ppm – black lines) as a function of temperature. Sensor exposure time to target gas is 4 minutes. Total flow is 200 mL/min.

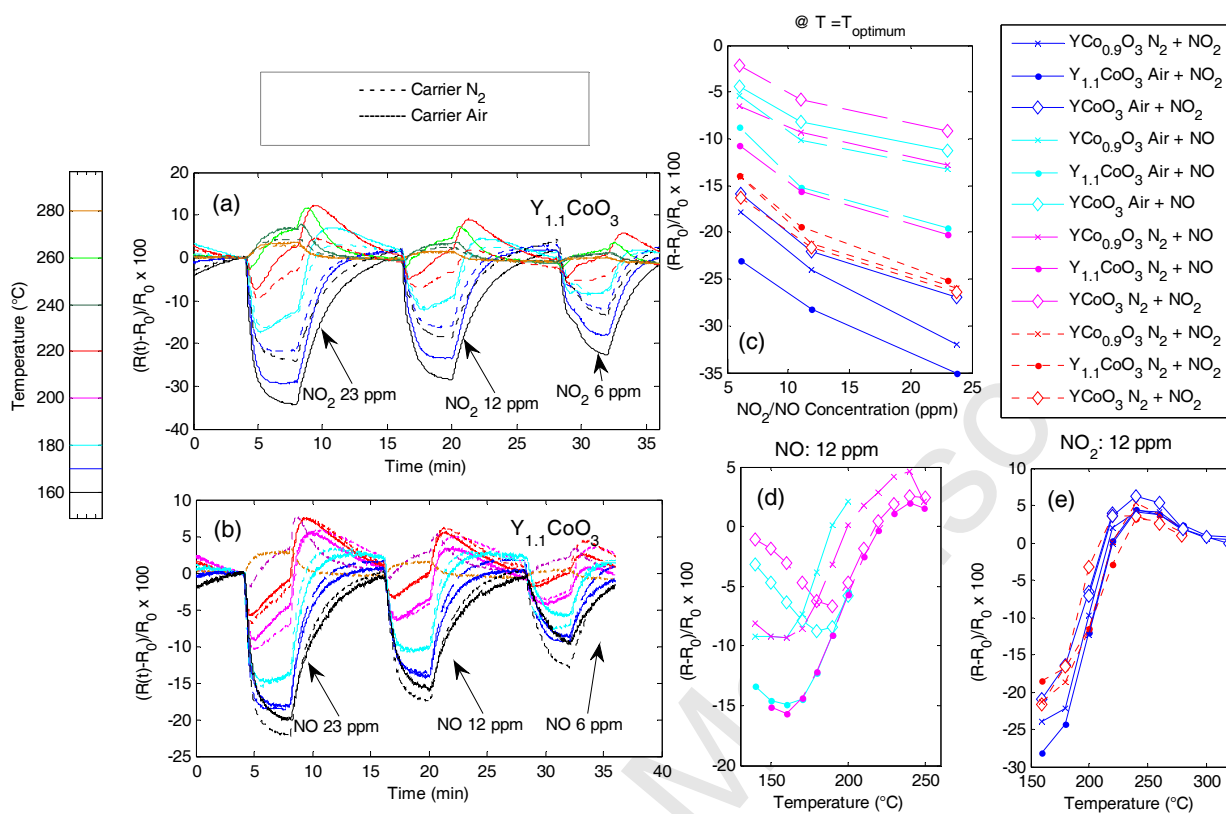


Figure 16. Response of the tested materials to NO_x . (a), (b): $Y_{1.1}CoO_3$ sensor responses versus time for different temperatures (between 160°C and 280°C) and for different carrier gases (air or nitrogen) to different NO_2 and NO concentrations, respectively; (c): response of the tested materials versus NO_x concentration at the optimum temperature (that is, the temperature where the response is maximum); (d), (e): responses of the tested materials as a function of temperature to a mixture of air/nitrogen and 12 ppm of NO and NO_2 , respectively. Sensor exposure time to target gas is 4 minutes. Total flow is 200 mL/min.

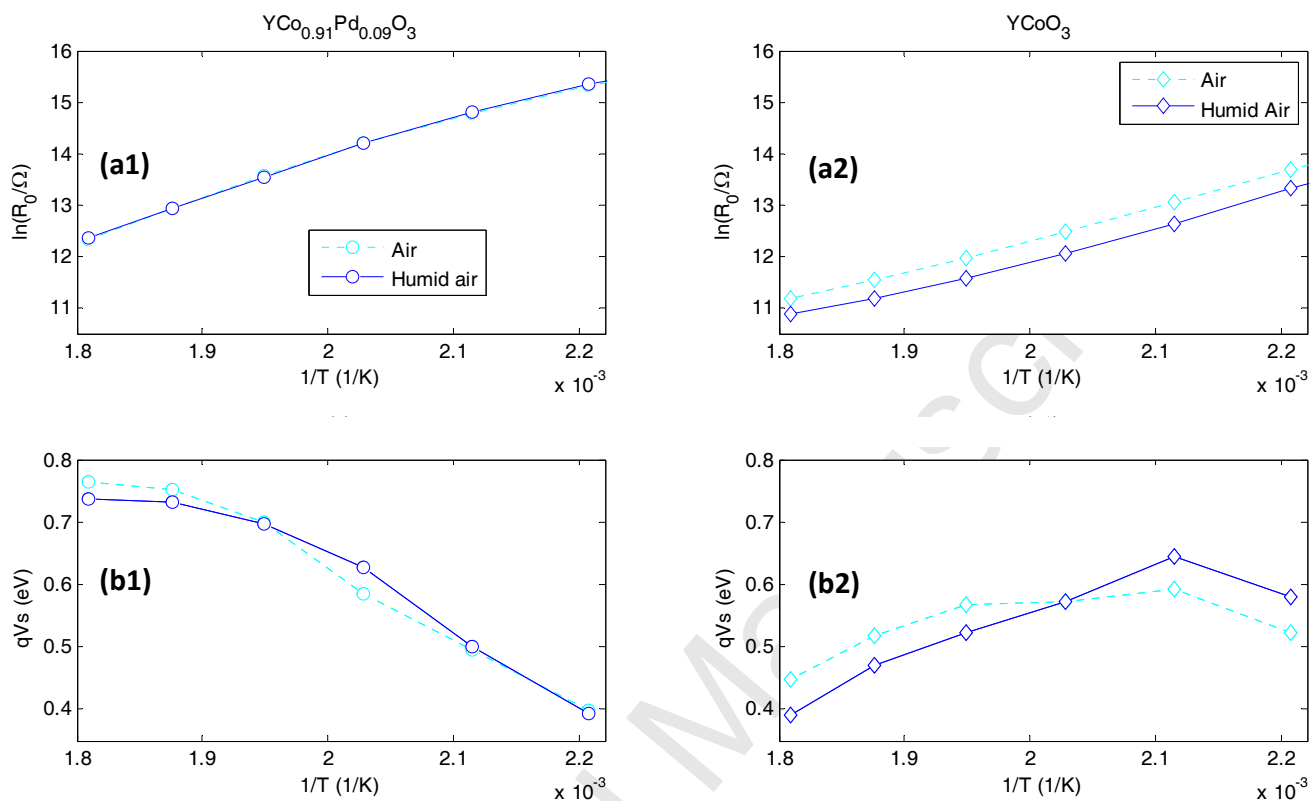


Figure 17. Upper plots: baseline resistance of $YCo_{0.91}Pd_{0.09}O_3$ (a1) and $YCoO_3$ (a2). Lower plots: estimated activation energy, in air and humid air (37% RH @ 25°C) for $YCo_{0.91}Pd_{0.09}O_3$ (b1) and $YCoO_3$ (b2).

Tommaso Addabbo received the Ph.D. degree in information engineering from the University of Siena, Italy, where he is currently working as a research associate. His main research interests include analysis of nonlinear circuits and systems, stochastic aspects of chaotic dynamics, and analog circuits design. During his research program, he was a Visiting Scholar at the Institute of Nonlinear Science at the University of California, San Diego, and at the Macedonian Academy of Sciences and Arts in Skopje, Macedonia.

Francesco Bertocci was born in Pescia, Italy, on February 18, 1980. He received the M.S. degree in Electronic Engineering in 2007 and the Ph.D. degree in Industrial and Reliability Engineering in 2011 from the University of Florence, Italy. His current research interests are design and development of different chemical sensors and their characterization through electrical and electronic instrumentation and measurements.

Ada Fort received the laurea degree in electronic engineering, in 1989 and the Ph.D. Degree in nondestructive testing in 1992, both from the University of Florence, Italy. She is currently an Associate Professor at the Department of Information Engineering, University of Siena, Italy. Her interests concern the development of measurement systems based on chemical and ultrasonic sensors and the development of automatic fault diagnosis systems. Recently, she has been involved in the study of random number generators based on chaotic maps.

Michele Gregorkiewicz holds a PhD in sciences from Technische Universität Darmstadt, Germany (1980). 1979 he collaborated as invited expert in the ionic conductivity group at Max-Planck-Institut für Festkörperforschung, Stuttgart, Germany. 1980-1992 he was research director for solid state chemistry and materials science at Instituto de Ciencia de Materiales, CSIC, Madrid, Spain. From 1994 he is professor of crystallography and materials science at Università di Siena. Current research interests include the crystallography and development of porous oxides exhibiting ionic and/or electronic conduction for applications in sensors, alternative energy and water desalination.

Marco Mugnaini received the Laurea degree in electronic engineering and the Ph.D. degree in reliability, availability, and logistics from the University of Florence, Florence, Italy, in 1999 and 2003, respectively.

Since 2003, he has been a Product Safety Engineer with General Electric Oil and Gas business, Florence, where he got his green belt certification. Since 2005, he has been an Assistant Professor with the Department of Information Engineering, University of Siena, Siena, Italy. His current interests include the development of measurement systems based on chemical sensors.

Roberto Spinicci has been an Associate Professor of chemistry at the Faculty of Engineering of the University of Florence, Florence, Italy. For many years he has been developing his research activity in the area of the heterogeneous catalytic reactions, focusing his attention mainly on the hydrocarbons and organic compounds oxidations and on the characterization of the investigated catalysts.

Valerio Vignoli received the laurea degree in electronic engineering from the University of Florence, Italy, in 1989, and the Ph.D. degree in nondestructive testing from the same university in 1994. Since 1997, he has been with the Department of Information Engineering, University of

Siena, Siena, Italy, where he is currently an Associate Professor of electronics. His recent research interests include the design of data acquisition and processing systems based on chemical sensors and the design of analog and mixed-signal electronic circuits.

Accepted Manuscript